

1 **Simulated microphysical properties of winter storms from bulk-type microphysics**
2 **schemes and their evaluation in the WRF (v4.1.3) model during the ICE-POP 2018**
3 **field campaign**

4
5 Jeong-Su Ko¹, Kyo-Sun Sunny Lim*¹, Kwonil Kim¹, GyuWon Lee¹, Gregory Thompson², and Alexis
6 Berne³
7

8 ¹School of Earth System Sciences, Center for Atmospheric Remote sensing (CARE), Kyungpook National
9 University, Daegu, Republic of Korea

10 ²National Center for Atmospheric Research, Boulder, CO, United States

11 ³Environmental Remote Sensing Laboratory (LTE), École Polytechnique Fédérale de Lausanne (EPFL),
12 Lausanne, Switzerland
13

14 ~~April 2022~~December 2021

15 (*submitted to GMD*)
16

17 *Correspondence: Kyo-Sun Sunny Lim (kyosunlim@knu.ac.kr)
18

변경된 필드 코드

서식 지정함: 영어(미국)

서식 지정함: 영어(미국)

19 **Abstract**

20 This study evaluates the performance of four bulk-type microphysics schemes, Weather Research and
21 Forecasting (WRF) Double-Moment 6-class (WDM6), WRF Double-Moment 7-class (WDM7), Thompson,
22 and Morrison, focusing on hydrometeors and microphysics budgets in the WRF model version 4.1.3. Eight
23 snowstorm cases, which can be subcategorized as cold-low, warm-low, and air-sea interaction cases,
24 depending on the synoptic environment during the International Collaborative Experiment held at the
25 Pyeongchang 2018 Olympics and Winter Paralympic Games (ICE-POP 2018) field campaign, are selected.
26 All simulations present a positive bias in the simulated surface precipitation for cold-low and warm-low cases.
27 Furthermore, the simulations for the warm-low cases show a higher probability of detection score than
28 simulations for the cold-low and air-sea interaction cases even though the simulations fail to capture the
29 accurate transition layer for wind direction. WDM6 and WDM7 simulate abundant cloud ice for the cold-low
30 and warm-low cases, so snow is mainly generated by aggregation. Meanwhile, Thompson and Morrison
31 simulate insignificant cloud ice amounts, especially over the lower atmosphere, where cloud water is
32 simulated instead. Snow in Thompson and Morrison is mainly formed by the accretion between snow and
33 cloud water and deposition. The melting process is analyzed as a key process to generate rain in all schemes.
34 The discovered positive precipitation bias for the warm-low and cold-low cases can be mitigated by reducing
35 the melting efficiency in all schemes~~by inefficient melting using all schemes~~. The contribution of melting to
36 rain production is reduced for the air-sea interaction case with decreased solid-phase hydrometeors and
37 increased cloud water in all simulations.

38 **Keywords:** Microphysics budgets, Hydrometeors, Snowfall, Bulk-type cloud microphysics, ICE-POP 2018.

40 1. Introduction

41 International Collaborative Experiments for Pyeongchang 2018 Olympic and Paralympic winter games (ICE-
42 POP 2018) field campaign was conducted over the Gangwon region, the northeastern part of the Korean
43 Peninsula during winter between 2017 and 2018. Various microphysical datasets in higher spatial and
44 temporal resolutions were collected during ICE-POP 2018 using X-band Doppler dual-polarization radar
45 (MXPoI), vertically pointing W-band Doppler cloud profiler (WProf), two dimensional video disdrometers
46 (2DVD) and PARticle Size VELOCITY (PARSIVEL) disdrometers, etc. Furthermore, numerical weather
47 prediction using various high-resolution models around the world was conducted to support weather forecasts
48 during the Olympic winter games as part of the Forecast Demonstration Project efforts of World Weather
49 Research Program in World Meteorological Organization. The analysis of collected observed data and high-
50 resolution modeling information during ICE-POP 2018 can improve our understanding of the snowfall
51 formation mechanism and related cloud microphysics processes over the complex terrain along the
52 mountainous region over Korea (Kim et al., 2021a; Gehring et al., 2020b; Gehring et al., 2021; Lim et al.,
53 2020; Jeoung et al., 2020).

54 Over the past decades, comparisons of microphysics schemes for simulating convection have been
55 performed, either on idealized testbeds (Morrison and Grabowski, 2007; Morrison and Milbrandt, 2011; Bao
56 et al., 2019) or real-world testbeds (Liu and Moncrieff, 2007; Luo et al., 2010; Han et al., 2013; Min et al.,
57 2015; Das et al., 2021). Han et al. (2013) evaluated cloud microphysics schemes for simulating winter storms
58 over California using observations from a space-borne radiometer and a ground-based precipitation profiling
59 radar. Simulations using four different cloud microphysics, Goddard, Weather Research and Forecasting
60 (WRF) single-moment 6-class scheme (WSM6), Thompson, and Morrison, showed a large variation in the
61 simulated radiative properties. All schemes overestimated precipitating ice aloft, and thus, positive biases in
62 the simulated microwave brightness temperature were found. The Morrison scheme presented the greatest
63 peak reflectivity due to snow intercept parameters. Min et al. (2015) reported that the experiment with the
64 WRF double-moment 6-class (WDM6) scheme shows better agreement with the radar observations for
65 summer monsoon over the Korean Peninsula compared to WSM6. Das et al. (2021) performed numerical

66 simulations over southwest India and concluded that the WDM6 microphysics scheme better simulates the
67 vertical convection structure of deep convection storms than the Morrison scheme and the Milbrandt-Yau
68 double-moment scheme and compare favorably to radar observations.

69 The aforementioned studies compared simulated precipitation, reflectivity, and storm structures using
70 different microphysics schemes under real-convection testbeds (Han et al., 2013; Min et al., 2015; Das et al.,
71 2021). Although these studies attempted to evaluate model performance using possible radar measurements,
72 they did not suggest microphysics pathways affecting the superiority of model performance. Recently, a few
73 studies have analyzed major microphysical pathways to cloud hydrometeor production, i.e., precipitation
74 (~~McMillen and Steenburgh 2015; Fan et al., 2017; Vignon et al., 2019; Huang et al., 2020; Lim et al., 2020~~).
75 ~~Through snowstorm simulations over the Great Salt Lake region, McMillen and Steenburgh (2015) reported~~
76 ~~that WDM6 generates more graupel and less snow with more total precipitation than Thompson scheme. The~~
77 ~~difference in graupel generation is due to WDM6's more efficient freezing of rain to graupel compared to~~
78 ~~Thomson. The amount of simulated graupel and snow efficiently affects precipitation efficiency for the~~
79 ~~selected snowstorm.~~ Fan et al. (2017) simulated mesoscale squall line with eight cloud microphysics schemes
80 in the WRF model and identified processes that contribute to the large variability in the simulated cloud and
81 precipitation properties of the squall line. They found that the simulated precipitation rates and updraft
82 velocities present significant variability among simulations with different schemes. Differences in ice
83 microphysics processes and collision-coalescence parameterizations between the schemes affected the
84 simulated updraft velocity and surface rainfall variability. Huang et al. (2020) presented simulation results of
85 WSM6, Thompson, and Morrison microphysics schemes for the severe rainfall case in the coastal
86 metropolitan city of Guangzhou, China. The simulation using WSM6 scheme presented the most similar
87 feature of precipitation with the observation in terms of intensity and distribution. Heating and cooling rate by
88 condensation and evaporation processes led to the difference of storm development and precipitation among
89 the simulations.

90 Through the modeling and observational studies of winter storms, the major microphysics processes
91 affecting the characteristics of winter storms have been figured out (McMillen and Steenburgh, 2015; Lim et
92 al., 2020; Ma et al., 2021) and the cloud microphysics parameterizations have been evaluated by utilizing the

93 measurements from extensive observation campaigns (Solomon et al., 2009; Molthan and Colle, 2012;
94 Conrick and Mass, 2019). Lim et al. (2020) ~~also~~ analyzed the microphysical pathway to generate hydrometeors
95 using WSM6 and WDM6 and showed that abundant cloud ice generation through the depositional process in
96 both schemes can be a reason for the positive precipitation bias during the winter season. Through snowstorm
97 simulations over the Great Salt Lake region, McMillen and Steenburgh (2015) reported that WDM6 generates
98 more graupel and less snow with more total precipitation than Thompson scheme. The difference in graupel
99 generation is due to WDM6's more efficient freezing of rain to graupel compared to Thomson. The amount
100 of simulated graupel and snow affects precipitation efficiency for the selected snowstorm. Ma et al. (2021)
101 emphasized that the cloud ice deposition/sublimation parameterization greatly affects to the snowfall amount.
102 By altering this parameterization in WSM6 scheme, the overestimation of the snowfall amount was notably
103 reduced in WRF simulations. Solomon et al. (2009) verified the microphysical characteristics for the simulated
104 mixed-phase clouds by utilizing the intensive measurements taken during the Mixed-Phase Arctic Cloud
105 Experiment (M-PACE). They showed that the double-moment microphysics scheme simulates realistic liquid
106 water paths, compared to the single-moment scheme. Through the comparison between the observation data
107 during The Canadian CloudSat/Cloud-Aerosol Lidar and Infrared Pathfinder Satellite Observations
108 (CALIPSO) Validation Project (C3VP) and assumptions used in microphysics schemes, Molthan and Colle
109 (2012) concluded that single-moment schemes having a flexibility in size distribution parameters as functions
110 of temperature can represent the vertical variability as observed ones from aircraft data. Conrick and Mass
111 (2019) evaluated Thompson microphysics scheme in the WRF model using observations collected during the
112 Olympic Mountains Experiment (OLYMPEX) field campaign by the Global Precipitation Measurement
113 (GPM) satellite and showed that Thompson scheme underpredicts radar reflectivity below 2 km and
114 overpredicts one above 2 km, consistent with the vertical mixing ratio profiles from GPM Microwave Imager.

115 Although major microphysics processes have been explored in a certain convection environment in
116 previous studies, simulated hydrometeor profiles have not been evaluated with the observation. Therefore, we
117 cannot determine whether the analyzed microphysical pathway is plausible. The purpose of this study is to
118 compare simulated hydrometeors and microphysics budgets as well as precipitation using different bulk-type
119 cloud microphysics schemes and evaluate the results with the possible observations during the ICE-POP 2018

120 field campaign. Furthermore, our study aims to estimate which microphysical pathway is possible under a
121 certain synoptic circumstance, which can be feasible by evaluating hydrometeor profiles with the observations.
122 This study is organized as follows. Section 2 describes the observation data used in this study and model
123 design with the case description. Results and summary are presented in sections 3 and 4, respectively.

124

125 **2. Experimental setup**

126 **2.1. Case description**

127 The eight snowfall events during the ICE-POP 2018 field campaign are selected in our study. Kim et al. (2021a)
128 classified the eight cases into three categories, namely, cold-low, warm-low, and air-sea interaction, according
129 to synoptic characteristics. A widespread snowfall can occur over the northeastern part of Korea during the
130 passage of a low-pressure system (LPS) over the Korean Peninsula (Nam et al., 2014; Gehring et al., 2020b).
131 Snowfall cases, categorized as a cold-low type, occur when the LPS located in the north of the polar jet
132 produces precipitation in the middle of the Korean Peninsula. These cases are featured with the predominant
133 westerly flow from the ground level to the cloud top (Kim et al., 2021a). From the thorough visual inspection
134 of sea-level pressure pattern, radar composite images, and accumulated precipitation distribution at the ground,
135 CASES 1 and 3 are categorized as a cold-low type (Table 1).

136 When the LPS located in the south of the polar jet passes over the southern part of Korea, widespread
137 precipitation can occur over the southern and middle parts of the Korean Peninsula. Kim et al. (2021a)
138 classified snowfall cases occurring under this synoptic situation as a warm-low type. One of the most
139 significant characteristics of this pattern is the two different vertical layers (Tsai et al., 2018; Kim et al., 2018;
140 Kim et al., 2021a; Kim et al., 2021b): the deep system aloft (~10 km height) is associated with LPS widespread
141 precipitation with the westerly flow, whereas the other snowstorm below is associated with sea-effect snow
142 with the easterly or northeasterly flow (Kor'easterlies, hereafter) (Park et al., 2020). Thus, the seeder-feeder
143 effect is expected in this type of precipitation systems. This vertical structure is maintained until the LPS-
144 related widespread precipitation moves further east to the East Sea or Japan, followed by the shallow

145 precipitation system with the Kor'easterlies-induced snow. Five warm-low events, CASES 2, 4, 5, 6, and 8 in
146 Table 1 were identified during the field campaign.

147 Snowfall cases associated with the air-sea interaction occur, accompanied by the Siberian high expansion
148 toward Kaema Plateau and/or East Sea. As the cold air from the north flows over the warm East Sea, a snow
149 cloud is formed (Veals et al., 2019; Steenburgh and Nakai, 2020), and it is advected by the Kor'easterlies,
150 resulting in frequent snowfall over the northeastern part of Korea. The depth of the snowfall system is
151 generally shallower (less than ~3 km height) than other types and is determined by the depth of the
152 Kor'easterlies layer and the height of the thermal inversion layer above. The air-sea interaction is the most
153 frequent synoptic scenario to produce heavy snowfall in the northeastern part of the Korean Peninsula (Cheong
154 et al., 2006; Choi and Kim, 2010; Kim et al., 2021a). However, only one event, CASE 7 in Table 1, is identified
155 during the ICE-POP 2018 field campaign. Our study selects CASES 3, 6, and 7 as representative cases for the
156 cold-low, warm-low, and air-sea interaction categories, respectively. A more detailed explanation of the
157 characteristics of each category is provided in Kim et al. (2021a).

158 2.2. Observation data

159 The observed precipitation from the Korea Meteorological Administration Automatic Weather Station (AWS)
160 during the analysis period for CASE 3, CASE 6, and CASE 7 is shown in Figure 1. A heated tipping-bucket
161 gauge was located on each station. The forecast and analysis period for each case is noted in Table 1 with the
162 total accumulated rain [mm] and the maximum rain rates [mm h^{-1}] during the analysis period. The spatial
163 distribution of surface precipitation in CASE 3 is rather uniform (Fig. 1a), producing a maximum rain rate of
164 2.41 mm h^{-1} . ~~For CASE 6, surface precipitation is concentrated in the southeastern and coastal regions~~
165 ~~For CASE 6, abundant precipitation amounts are shown in southeastern region and along the coastal region~~ (Figs.
166 1b). The maximum rain rate along the coastal region is shown in CASE 7 (air-sea interaction). The observed
167 maximum rain rate is 3.9 mm h^{-1} for CASE 6 and 4.87 mm h^{-1} for CASE 7. The greatest amount of
168 precipitation is observed with CASE 4 (warm-low), and the least one with CASE 3 (cold-low) among the
169 eight cases (Table 1).

170 Accurate measurement of precipitation by a heated tipping-bucket gauge is a challenge in windy
171 environment. Strong winds lead to severe undercatch of snowfall amount in particular for a solid precipitation
172 (Goodison et al., 1998; Thompson and Eidhammer, 2014; Kochendorfer et al., 2017; Smith et al., 2020). Other
173 sources of measurement uncertainty include sublimation or evaporation on the heated gauge funnel
174 (Rasmussen et al., 2012), orifice capping during heavy snowfall (Boudala et al., 2014), blowing snow (Geerts
175 et al., 2015), and representativeness of the observation particularly in the mountainous region. Hence, it should
176 be noted that the precipitation amount analyzed in this study may suffer from these sources of uncertainty,
177 likely resulting in less precipitation amount. Despite these limitations, this study takes an advantage of dense
178 network of heated tipping-bucket gauges, which was comprised of 129 stations within the studied area of
179 about $160 \times 200 \text{ km}^2$. In addition, all gauges were equipped with a single shield that improves catch efficiency
180 of snow in windy condition (Kochendorfer et al., 2017).

181 During the ICE-POP 2018 field campaign, remote-sensing, and in situ measurements for cloud properties
182 were performed over the northeastern part of South Korea. The Gangneung-Wonju National University (GWU)
183 marked with a closed red square in Figure 1a represents the coastal observation site. DaeGwallyeong regional
184 Weather office (DGW), MayHills Supersite (MHS), and BoKwang 1-ri Community Center (BKC) are the
185 mountain observation sites, which are represented as an open circle and a closed triangle sign in Figure 1a.
186 PARSIVEL disdrometers (Löffler-Mang and Joss, 2000; Tokay et al., 2014) at the GWU and DGW sites
187 provide the frequency distributions of particle fall velocity as functions of diameter at the surface; thus, we
188 can obtain the information about the surface precipitation type for each representative case, as shown in Figure
189 2. At the coastal site, GWU, a mixture of snow and liquid-type precipitation is measured for CASE 3. CASE
190 6 is characterized by the liquid-type and graupel-like precipitation, and CASE 7 consists of the liquid-type
191 precipitation. At the mountain site, DGW, a mixture of liquid-type precipitation with snow and graupel is
192 observed in all cases, but a more intense signal of the liquid-type precipitation is seen in CASE 7.

193 The MXPoI radar measurement, located at the GWU site, provides the classified hydrometeor
194 information along the direction between MHS and GWU. Figure 3 shows the area of hydrometeor types in
195 which the hourly average fraction is larger than the threshold. The period is selected for the peak time of the

196 domain-averaged rain— for each case. The radar-classified hydrometeors are 8 hydrometeor types based on
197 the algorithm proposed by Besic et al. (2016, 2018): crystals (CR), aggregates (AG), light rain (LR), rain (RN),
198 rimed ice particles (RP), wet snow (WS), ice hail and high-density graupel (IH), and melting hail (MH). The
199 hydrometeors are not drawn over the region, where radar echoes are absent.

200 CR is the primary hydrometeor type, and AG is between 1.5 and 3.0-km level in CASE3 (Fig. 3a). For
201 CASE6, CR is also the major hydrometeor type over the entire observational region. A small portion of AG
202 exists around the coastal GWU site at the 0.5-km level (Fig.3b). Hydrometeors are mainly classified into CR,
203 AG with a small portion of RP above the 0.5-km level, and WS/LR below the 0.5-km level from the
204 observation for CASE 7 (Fig. 3c). The freezing level is drawn using the radiosonde observations at BKC site
205 on 09 UTC 22 Jan, 00 UTC 08 Mar, and 15 UTC 15 MAR for each case. The retrieved wind fields (cross-
206 barrier and vertical wind) from multiple surveillance Doppler radars (Liou and Chang, 2009; Tsai et al., 2018)
207 are also represented in Figure 3. The wind fields are the hourly averaged ones during the 1-h time window,
208 centered at the maximum precipitation time. The westerly winds generally blow from mountains to the ocean
209 and become stronger with higher altitude in CASE 3. Both CASESs 6 and 7 show the transition zone of wind
210 fields, northeasterly below and southwesterly above. In general, the flow patterns well follow the overall
211 characteristic of winds for three types of precipitation systems (see Kim et al. 2021a).

212 2.3. Model design

213 The Advanced Research WRF model version 4.1.3 (Skamarock et al., 2008) is used for simulations. The WRF
214 model is a nonhydrostatic, compressible model with an Arakawa-C grid system and has several options for
215 each physics parameterization. The model grids consist of three nested domains with a horizontal grid spacing
216 of 9, 3, 1 km (Fig. 4). The 65 vertical levels are configured with a 50-hPa model top. Table 2 shows the
217 summary of the model configuration, including the number of model grids, the physics parameterization used,
218 and initial/boundary conditions for model integration. The Kain-Fritsch (Kain and Fritsch, 1990; Kain, 2004)
219 scheme is only applied to the outer domain of the 9-km resolution domain. The model forecast and analysis
220 periods for each case are listed in Table 1. The model results are evaluated over the Yeongdong area of
221 northeastern South Korea during the analysis period, represented as a dotted square in Figure 4.

Four cloud microphysics parameterizations, namely, WDM6 (Lim and Hong, 2010), WRF Double-Moment 7-class (WDM7) (Bae et al., 2019), Thompson (Thompson et al., 2008), and Morrison (Morrison et al., 2005), are used in our study. WDM6 and WDM7 schemes include the corrections for the numerical errors in ice microphysics parameterizations (Kim and Lim, 2021) and for cloud evaporation and melting processes (Lei et al., 2020). WDM6, Thompson, and Morrison parameterizations include five hydrometeor types such as cloud water, rain, ice, snow, and graupel. WDM7 is developed on the basis of WDM6 by adding the prognostic variable of hail mixing ratio. WDM6 and WDM7 predict both number concentration and the mixing ratio for liquid particles but only the mixing ratio for solid-phase hydrometeors. Thompson predicts the number concentration and the mixing ratio for ice and rain but only the mixing ratio for other hydrometeors. In Morrison, the number concentration and the mixing ratio are predicted for all hydrometeors, except for cloud water, for which only the mixing ratio is predicted. There exist the aerosol-aware versions of Thompson and Morrison schemes in the WRF model. However, we perform the model simulations using Thompson and Morrison schemes, which do not include the aerosol activation processes; thus, two schemes do not predict the cloud water number concentration. Table 3 shows the prognostic variables for each microphysics scheme. The tested parameterizations are full or partially double-moment schemes, as shown in Table 3. For the microphysics budget analysis, the name of the source/sink terms in each microphysics scheme, differently designated, is matched, as shown in Table 4. For example, the cloud water condensation/evaporation process from all microphysics schemes is identically denoted as QCCON.

3. Results

3.1. Cold-low case

The simulation results for cold-low cases are presented in this section. Figure 5 shows the statistical skill scores of bias, root mean square error (RMSE), probability of detection (POD), and false alarm ratio (FAR) for the simulated precipitation using the WDM6, WDM7, Thompson, and Morrison schemes. White, black, yellow, and blue-colored bars represent the results for the simulations with the WDM6, Thompson, and

247 Morrison schemes. The cold-low, warm-low, and air-sea interaction cases are shaded in blue, red, and green
248 color. We adopt the threshold value of 0.05 mm h^{-1} to judge the existence of precipitation when calculate
249 POD and FAR. The calculation method of POD and FAR follows the study of Rezacova et al. (2009). All
250 microphysics parameterizations present a positive bias for against the surface precipitation~~overestimate the~~
251 ~~surface precipitation amount.~~ Thompson and Morrison simulations show better skill scores in bias, RMSE,
252 and FAR, compared to WDM6 and WDM7. The accumulated precipitation during the analysis period for
253 CASE 3, the representative case of the cold-low type, is shown in Figures 6a–d. All schemes simulate the
254 precipitation as a type of snow ~~and rain~~ over the northeastern part of the domain. WDM6 and WDM7 simulate
255 more liquid rain at the surface precipitation than Morrison and Thompson. Simulated hydrometeor types at
256 the surface are compared qualitatively with measurements using PARSIVEL disdrometers (Fig. 2). In CASE
257 3, the simulated hydrometeor types are snow and rain over the coast and mountains in all schemes (Figs. 6a–
258 d). Although graupel-type precipitation is not predicted at the surface in all schemes, the overall feature
259 matches well with the observation (Figs. 2a and d).

260 When the strongest domain-averaged precipitation intensity is observed, the simulated hydrometeors and
261 wind are compared with the retrieved ones from radars along the cross-section between GWU and MHS sites
262 (Figs. 3a and 7a–d). For the comparison analysis, hydrometeor types of CR, AG, and IH from the retrievals
263 can be regarded as cloud ice, snow, and hail in the model. The hydrometeor type of RP can be corresponded
264 to graupel in the model. RN and MH can be considered rain in the model, and LR as cloud water or rain. WS
265 is not predicted by any of the microphysics schemes verified in our study. WDM6 and WDM7 simulate cloud
266 ice over the entire region of the cross-section above 2-km level. Furthermore, cloud ice is predicted, even near
267 the mountain top, with a snow amount greater than 0.38 g kg^{-1} at around 1.5-km level~~with a substantial snow~~
268 ~~amount.~~ However, both schemes miss the observed snow near GWU site. Thompson and Morrison also
269 simulate sufficient snow mass, showing its maximum near the mountain top. However, cloud ice is not
270 simulated with both schemes. This is because Thompson and Morrison schemes efficiently transfer cloud ice
271 to snow at the cut-off diameter of 200 and 250 μm , therefore the schemes keep all cloud ice size relatively
272 small. Over the mountain top where cloud ice is shown in WDM6 and WDM7, cloud water is simulated with

273 Morrison and Thompson instead. More cloud ice with WDM6 and WDM7 can be also confirmed in the time-
274 domain averaged vertical profiles of hydrometeors (Fig. 8). As shown in Figures 8a and b, the vertical
275 distributions of hydrometeors from WDM6 and WDM7 are comparable in terms of the vertical extent and the
276 maximum level of hydrometeors similar, except hail. WDM7 simulates more hail as much as decreased snow.
277 Thompson rarely produces ice and shows the largest snow amount among the schemes used in the experiments.
278 Morrison simulates cloud ice in layers between 3-and 6-km levels. ~~Meanwhile, the sum of cloud ice and snow,~~
279 ~~drawn in a red line, shows a similar amount in all schemes.~~ Consistently with the hydrometeor distribution
280 shown from the cross-section, Thompson and Morrison produce more cloud water below 4-km level than
281 WDM6 and WDM7 (Figs. 8c and d). In all experiments, the simulated winds blow from the inland to the
282 ocean, consistently shown from the observation (Figs. 3a and 7a–d). Meanwhile, the simulated winds are
283 weaker than the observation over the mountainous areas.

284 The relative contribution of microphysics processes in the production of each hydrometeor is compared
285 among experiments in Figure 9. The production rate of microphysical processes is averaged over the same
286 analysis domain and duration, as considered in the precipitation and hydrometeor analysis shown in Figures
287 5 and 6. The absolute values of every production rate to generate or dissipate a certain hydrometeor are
288 summed, and each production rate is divided by the sum to generate a percentage. The positive rates in Figure
289 9 indicate source processes for the hydrometeor, and the negative rates indicate sink ones. The contribution
290 of sedimentation could be indirectly estimated from the hydrometeor mixing ratio and cloud microphysics
291 budget amount. The cloud condensation nuclei (CCN) activation process (QCGEN) is the main source of
292 cloud water in WDM6 and WDM7 (Figs. 9a–b). Meanwhile, cloud water in Thompson and Morrison is
293 primarily generated by QCCON due to the absence of QCGEN (Figs. 9c–d). QCGEN includes only the
294 condensation, but QCCON includes both condensation and evaporation. The negative sign of QCCON means
295 that the magnitude of evaporation is greater than that of condensation. Note that we use the non-aerosol-aware
296 version of the Thompson and Morrison scheme, which excludes aerosols and related microphysics processes.
297 The collision/coalescence between cloud water and other hydrometeors (QCACR, QCACS, and QCACG) is
298 the main sink for cloud water in all schemes. Besides these accretions, evaporation is another major sink of

cloud water in WDM6 and WDM7. Most of the rain is produced by melting from solid-phase hydrometeors (QRMLT) (Figs. 9e–h) in all experiments and consumed by the evaporation process (QRCON), except for Thompson.

The deposition/sublimation of water vapor to cloud ice (QIDEP) is the primary source of cloud ice (Figs. 9i–l). Cloud ice decreases as it is converted into snow due to the auto-conversion process (QSAUT) and collision/coalescence process with snow (QIACS). The main processes to generate or deplete cloud ice are identical in all microphysics schemes. However, the absolute magnitude of QIDEP in WDM6 and WDM7, that is, approximately 1.4 g kg^{-1} , is greater than that in Morrison and Thompson, approximately 0.05 g kg^{-1} , leading to more cloud ice generation. In WDM6 and WDM7, most of the snow is produced by QSAUT and QIACS, but in Morrison, it is produced by QCACS and deposition from water vapor to snow (QSDEP) (Figs. 9 m–o). QCACS is the primary source of snow in Thompson as well (Fig. 9p). Snow is depleted by a melting process (QSMLT) in all simulations. The accretion between snow and hail (QSACH) is also the primary sink of snow in WDM7. Meanwhile, graupel is mainly produced by the accretion process, QCACG, in WDM6(7) and Morrison. However, in Thompson, graupel is mainly produced by the freezing process (QGFRZ) and QCACS. WDM7, predicting hail additionally, shows that the collision/coalescence between graupel and hail (QGACH) and QSACH are the major processes for hail generation. Meanwhile, Jang et al. (2021) showed that QGACH and QSACH can be eliminated by applying the mass-weighted terminal velocity for hail following the method by Dudhia et al. (2008); thus, the hail generation considerably decreases.

Except for the major sinks of graupel and snow, QGACH and QSACH, the responsible microphysical processes for generating hydrometeors in WDM6 and WDM7 are similar. The inclusion of aerosols in the microphysics processes causes the difference in major source/sink of cloud water, which can be seen from the comparison between WDM6(7) and Morrison/Thompson. In addition, more efficient cloud ice and inefficient cloud water production in WDM6(7), compared to others, cause the difference in the primary microphysics processes for snow production. Kim et al. (2021a) estimated possible microphysical processes from the measured particle size distribution and diameter for the cold-low case during ICE-POP 2018. Both aggregation and riming are analyzed as major processes to produce snow at the mountain site. Our analysis shows that

325 aggregation is preferred in WDM6(7) and riming in Thompson and Morrison at the top of the mountain (Figs.
326 7a–d). In addition, the enhanced melting of solid-phase particles in WDM6(7), compared to Thompson,
327 produces much rain, resulting in a larger positive bias of simulated precipitation.

328 3.2. Warm-low case

329 Simulated precipitation, hydrometeors, and microphysics budgets are compared for the warm-low cases in
330 this section. The warm-low category includes five cases such as CASES 2, 4, 5, 6, and 8. Overall, all
331 simulations in the warm-low category show better POD and FAR than those in the cold-low category, except
332 FAR for CASE 8. Consistent with the simulations for the cold-low category, all simulations in the warm-low
333 category present a positive bias of surface precipitation, except CASE 4 with WDM7 (Fig. 5). WDM6 overall
334 shows the best bias scores. Morrison shows the best POD score, but the worst bias, RMSE, and FAR, by
335 producing abundant precipitation, except for CASE 5. All simulations show the worst bias and RMSE scores
336 for CASE 5 among the warm-low cases. WDM6, Thompson, and Morrison simulate the surface precipitation
337 type as rain and snow (Figs. 6e, g, and h). However, WDM7 simulates hail-type precipitation amount more
338 than 10 mm abundant hail-type precipitation over the southeastern part of the analysis domain. Jang et al (2021)
339 noted that WDM7 generates too much hail regardless of the simulated convections. The area receiving the
340 snow-type precipitation is confined in a narrow mountain region with WDM7 (Fig. 6f). The simulated
341 hydrometeor types in all simulations are inconsistent with the observations, especially over the coastal region.
342 The observation certainly shows graupel-like precipitation over the coastal region (Fig. 2b).

343 Figures 7e–h shows the simulated hydrometeors and wind fields for CASE 6 when the strongest domain-
344 averaged precipitation intensity is observed. The simulated cloud ice appears just above the freezing level in
345 WDM6 and WDM7. WDM7 simulates the freezing level lower than other schemes, which is not consistent
346 with the observation (Figs. 7f and 3b). Meanwhile, Thompson and Morrison simulate a large amount of snow
347 above the surface with an absence of cloud ice because these schemes only allow the relatively small size of
348 cloud ice. WDM7, Thompson, and Morrison simulate cloud water below the 0.5-km level over the coast. The
349 vertical profiles of the time-domain averaged hydrometeors present more snow and cloud water with
350 Thompson and Morrison (Fig. 10cd). Figure 10 also shows that WDM6 and WDM7 simulate more cloud ice

351 between the 10-km level and surface than other schemes. Morrison produces cloud ice between the 6- and 12-
352 km levels, and Thompson simulates a little cloud ice amount. However, the sum of snow and cloud ice amount
353 is greatest in Thompson. All cloud ice in Thompson scheme is relatively smallest, therefore its mixing ratio
354 can be nearly always an order of magnitude or more less than other schemes. Kim et al. (2021a) mentioned
355 that snowfall cases belonging to the warm-low category show the deepest system and precipitation are
356 enhanced by the seeder–feeder mechanism with two different precipitation systems divided by wind fields,
357 easterly below and westerly above. However, the transition layer of wind direction in all simulations is located
358 at the higher latitude, relative to the observed layer (compare Figs. 7e–h and 3b), which can cause a deficiency
359 in simulating related microphysical mechanisms.

360 The relative contribution of microphysical processes to generate each hydrometeor among the schemes
361 is compared in Figure 11. QCGEN and QCCON are the primary sources for cloud water in WDM6(7) and
362 Thompson/Morrison, respectively. The contribution of QRWET, responsible for generating rain, is reduced
363 with WDM7 for the warm-low case, compared to the cold-low case. QRMLT is still the primary source of
364 rain in all simulations (Figs. 11 e–h). The major sinks and sources of the liquid hydrometeors are ~~similar~~
365 identical between the warm-low and cold-low cases. The responsible microphysical processes for cloud ice
366 formation and depletion are also identical to those for the cold-low case (Figs. 11i–l). The main source of
367 cloud ice is QIDEP in all simulations. The magnitude of QIDEP in WDM6 and WDM7 is 5.5 g kg^{-1} , which
368 is approximately 10 times larger than that of Morrison and Thompson, leading to an abundant production of
369 cloud ice greater than 0.06 g kg^{-1} (Fig. 10ab).

370 The melting processes (QSMLT, QGMLT, and QHMLT) are the primary sinks of solid-phase
371 precipitating particles such as snow, graupel, and hail in all simulations. The relative contribution of melting
372 for the warm-low case, CASE 6, is greater than that for the cold-low case, CASE 3, due to the warm
373 environment and the extended vertical range of solid-phase hydrometeors (Figs. 10m–u). All simulations show
374 that the magnitude of QRMLT in CASE 6 is approximately 10 times larger than that in CASE 3. The melting
375 process can largely affect rain production, resulting in surface precipitation in the warm-low case. The
376 contribution of QCACS to snow generation is significantly decreased in Thompson and Morrison in the warm-

low case compared to the cold-low case. This is because of the reduced cloud water in CASE 6 with Thompson and Morrison, compared to the CASE 3. In both schemes, cloud water generation is suppressed in the warm-low case. Even though both QSAUT and QIACS are still the major sources of snow production in WDM6(7), the contribution of QSAUT decreases, and that of QIACS increases in WDM6 and WDM7 in the warm-low case compared to the cold-low case. There is no distinct discrepancy for the key microphysical processes of graupel (and hail) formation and depletion between the warm-low and cold-low cases.

3.3. Air-sea interaction case

Statistical skill scores for the simulated precipitation are presented in Figure 5 for the air-sea interaction case. Only one case, CASE 7, is classified as an air-sea interaction category during the ICE-POP 2018 field campaign, presenting a negative bias. Overall, Morrison shows the best skill scores for the simulated precipitation. The POD from simulations with WDM6 and WDM7 show the worst scores due to the missing precipitation events over the southwestern part of the analysis domain (Figs. 1c and 6i, j). The precipitation system, which is initiated by air-mass transformation over the East Sea, propagates to inland areas by the easterly winds. Therefore, the precipitation area is restricted in the eastern area of the Korean Peninsula and intense precipitation is presented along the coast in both the observation and simulations (Figs. 6i–l). WDM6 and WDM7 simulate ~~abundant~~ solid-phase precipitation amounts more than 14 mm compared with the ~~simulations with Thompson and Morrison~~. In addition, WDM7 produces hail-type precipitation over the coast. The precipitation type simulated with WDM6 and WDM7 does not match with the observed types, especially over the coast (Figs. 2 and 6i–l). Observation shows pure liquid-type precipitation, but both simulations produce excess solid-phase precipitation.

The simulated hydrometeor distribution and wind fields over the cross-section are compared to the observations (Figs. 3 and 7i–l). When the strongest domain-averaged precipitation intensity is observed, all simulations produce a significant amount of cloud water below the 3-km level. A large amount of cloud water in the simulations can be also confirmed in the time-domain averaged vertical profiles of hydrometeors (Fig. 12). In all simulations, simulated hydrometeors are confined to below the 4-km level. WDM6 and WDM7 produce the largest amount of cloud water and cloud ice/snow. The experiment with Morrison simulates more

403 rain than other simulations (Fig. 12d). WDM6 and WDM7 simulate cloud ice with some snow and graupel
404 below the 2-km level, which is consistent with the observation in which CR, AG, and RP are seen (Figs. 3 and
405 7i, j). However, the region with the graupel (RP in the observation) is shifted to the coastal region in WDM6
406 and WDM7, generating excess solid-phase precipitation over the coast. Consistent with other cases,
407 Thompson and Morrison do not simulate cloud ice at the maximum precipitation time. Morrison simulates
408 snow between the surface and 2-km level, representing its maximum at the coastal GWU site (Fig. 847). All
409 experiments show the westerly wind over the ocean and coastal area, indicating that they fail to simulate the
410 Kor'easterlies, which is the most important dynamical characteristics of the air-sea interaction category.

411 Figure 13 shows the relative contribution of microphysical processes for CASE 7. Unlike the cold-low
412 and warm-low cases, cloud water is mainly depleted by QCACR in Thompson and Morrison due to decreased
413 snow production in the air-sea interaction case. The primary source and sink for cloud water are not changed
414 in WDM6 and WDM7. In all simulations, the relative contribution of QRMLT in the generation of rain
415 decreases, and the contribution of cloud water-to-rain processes such as QCACR, QRAUT, and QRWET
416 increases. In particular, QCACR and QRAUT are the main sources of rain in Thompson, and QCACR in
417 Morrison. For cloud ice, QIDEP and the generation of ice by nucleation and CCN activation (QIGEN) are
418 analyzed as the major sources in all simulations. The contribution of QIGEN in cloud ice production increases
419 compared to cold-low and warm-low cases. In WDM6 and WDM7 schemes, the magnitude of QIDEP is 0.27
420 g kg⁻¹, which is about 10 times larger than that in Thompson and Morrison. In all simulations, the relative
421 contribution of QCACS to the formation of snow increases due to increased cloud water generation, and those
422 of QIACS and QSAUT decrease with the decreased cloud ice generation. However, QIACS and QSAUT in
423 both WDM6 and WDM7 are still major sources of snow. ~~Both schemes simulate abundant cloud ice compared~~
424 ~~to Thompson and Morrison in CASE 7 as well.~~ In Morrison, the contribution of QSDEP to snow formation is
425 significantly reduced in the air-sea interaction case, unlike the cold-low and warm-low cases. Several
426 microphysics processes are involved in graupel formation with Thompson for the air-sea interaction case, but
427 the formed graupel amount is not identified in the surface precipitation insignificant.

4. Summary

This study evaluates the performance of the four microphysics parameterizations, WDM6, WDM7, Thompson, and Morrison, which have been widely used as cloud microphysics options in the WRF model, in simulating snowfall events during the ICE-POP 2018 field campaign. Eight snowfall events, classified into three categories (cold-low, warm-low, and air-sea interaction), depending on the synoptic characteristics, are selected. The evaluation is conducted focusing on the simulated hydrometeors, microphysics budgets, wind fields, and precipitation using the measurement data from MXPoI radar, multiple surveillance Doppler radars, PARSIVEL disdrometers, and AWS. Most simulations show a deficiency of a positive bias in the simulated precipitation for the cold-low and warm-low cases. The simulations for the air-sea interaction case present a negative bias and show the best bias score. Overall, the modeled precipitation for the warm-low cases shows a better POD score than that for the cold-low and air-sea interaction cases.

The simulated hydrometeor types at the surface for the cold-low case are snow and rain over both coastal and mountainous regions, regardless of the microphysics schemes, which is consistent with the observed features. Both WDM6 and WDM7 simulate an abundant amount of cloud ice and snow, especially over the mountain top and its downslope region when the strongest precipitation intensity is observed. The retrievals from the radar also ~~show-classify abundant~~ cloud ice and snow as primary hydrometeor types over the downslope region of the mountain top. Thompson and Morrison simulate sufficient snow amount; however, both do not produce cloud ice over the downslope region, because these schemes keep all cloud ice relatively small, compared to WDM6 and WDM7. In all experiments, the simulated winds blow from the inland to the ocean, as observed in the Doppler radar-retrieved one. Most rain mixing ratio is produced by melting in all experiments. The primary processes that generate or deplete cloud ice are identical in all microphysical schemes, which are the deposition for the formation and conversion to snow or collision/coalescence for depletion. Snow is mainly generated by aggregation in WDM6 and WDM7, but the accretion between snow and cloud water and deposition is mainly generated in Thompson and Morrison.

For the warm-low case, all experiments mainly produce rain and snow-type surface precipitation over the coastal and mountainous areas. WDM7 predicts hail-type precipitation amount more than 10 mm, which

455 ~~is not observed~~WDM7 ~~predicts abundant hail type precipitation~~. The simulated hydrometeor types in all
456 simulations are inconsistent with the observations, which shows graupel-like precipitation especially over the
457 coastal region. WDM6 and WDM7 simulate the ~~abundant~~ cloud ice amount between 0.01 and 0.1 g kg⁻¹ near
458 the coast site when the maximum precipitation is observed. Meanwhile, Morrison and Thompson simulate
459 ~~abundant more~~ snow over the corresponding region, compared to WDM6 and WDM7. Although the simulated
460 precipitation skill scores for the warm-low category are the best among all simulated categories, all
461 simulations have a problem, the lower wind- transition layer, compared to the observed-transition layer.
462 Through the microphysics budget analysis, it is found that the major sources and sinks of hydrometeors are
463 ~~similar-identical~~ between the cold-low and warm-low cases. Meanwhile, the magnitude of melting is
464 significantly enhanced in warm-low cases compared to cold-low cases, due to the warmer environment and
465 more available solid-phase hydrometeors. The relative contribution of collision/coalescence between cloud
466 water and snow to produce snow is decreased compared to cold-low cases in the simulations with Thompson
467 and Morrison, which is due to the reduced cloud water. For the air-sea interaction case, WDM6 and WDM7
468 simulate surface precipitation as a solid-phase type along the coast, which is inconsistent with the observation.
469 This is because WDM6 and WDM7 produce excessive cloud ice amount with graupel/snow over the coast. In
470 addition, none of the experiments simulate the low-level Kor'easterlies. Unlike the cold-low and warm-low
471 cases, simulations for the air-sea interaction case produce abundant cloud water amount greater than 0.2 g kg⁻¹
472 ¹ abundant cloud water. Therefore, rain is greatly generated by cloud collision/coalescence of cloud water, not
473 primarily from melting.

474 More cloud ice generation with WDM6 and WDM7 and more cloud water generation with the Morrison
475 and Thompson schemes are distinct in all cases. Therefore, the major microphysical processes to generate
476 snow are significantly related with cloud ice in WDM6 and WDM7, and with cloud water in Morrison and
477 Thompson. Thompson (or Morrison) scheme transfers the cloud ice to snow at the diameter of 200 (or 250)
478 μm , therefore more snow exists relative to WDM6 and WDM7 schemes, in which the maximum allowable
479 diameter of cloud ice is 500 μm . Melting is the major process to produce rain in warm-low and cold-low cases.
480 Therefore, the positive precipitation bias revealed from the warm-low and cold-low cases can be mitigated by

481 modulating the melting efficiency in all schemes. Microphysics budget analysis shows that the inclusion of
482 the prognostic variable of CCN number concentration changes the major source of cloud water production.
483 CCN activation is the major process to produce cloud water with WDM6 and WDM7, with the CCN number
484 concentration serving as a prognostic variable, but the condensation is the major process for cloud water
485 generation with Morrison and Thompson. Our study also shows that the additional prognostic variable of hail
486 has no advantage in simulating precipitation and hydrometeor profiles and produces excessive hail at the
487 surface for the snowfall event that occurs over the complex terrain region in the eastern part of the Korean
488 Peninsula. Even though several studies simulated snow storm cases under the horizontal resolution of 1-km
489 or 1.33 km (Alcott and Steenburgh, 2013; Molthan et al., 2016; Vignon et al., 2019; Veals et al., 2020), the 1-
490 km horizontal resolution, used in our study, could be coarse for some generating cells during winter season.
491 However, these small-scale cells cannot alter the major findings of our study.

492
493 *Code and data availability.* The WRF model version 4.1.3 is available at [https://github.com/wrf-](https://github.com/wrf-model/WRF/releases)
494 [model/WRF/releases](https://github.com/wrf-model/WRF/releases) (last access: January 2022). The ERA-Interim reanalysis data from the European Centre
495 for Medium-Range Weather Forecasts (ECMWF) for initial and boundary conditions is available at
496 <https://apps.ecmwf.int/datasets/data/interim-full-daily/levtype=pl/> and
497 <https://apps.ecmwf.int/datasets/data/interim-full-daily/levtype=sfc/> (last access: October 2019). The model
498 codes and scripts and that cover every data and figure processing action for all the results reported in this
499 paper are available at https://zenodo.org/record/5876054#.YefSK_5BwuU. The observational data such as
500 Parsivel and MXPol radar are available via <http://dx.doi.org/10.5067/GPMGV/ICEPOP/APU/DATA101> and
501 <https://doi.org/10.1594/PANGAEA.918315>. - Model outputs are available upon the request (Jeong-Su Ko via
502 jisko@knu.ac.kr).

503
504 *Author contributions.* JK designed and performed the model simulations and analysis under the supervision
505 of KL. KL and JK wrote the manuscript with substantial contributions from all co-authors. KK processed the

506 observational data. KL, GL, AB, and GT contributed to the scientific discussions and gave constructive advice.

507 KK and AB carried out the PARSIVEL and Radar measurements.

508

509 *Competing interests.* The authors declare that they have no conflict of interest.

510

511 *Special issue statement.* This article is part of the special issue “Winter weather research in complex terrain
512 during ICE-POP 2018 (International Collaborative Experiments for PyeongChang 2018 Olympic and
513 Paralympic winter games) (ACP/AMT/GMD inter-journal SI)”. It is not associated with a conference.

514

515 *Funding.* This work was supported by the National Research Foundation of Korea (NRF) grant funded by the
516 Korean government (MSIT) (No. 2021R1A4A1032646)

517

518 *Acknowledgments.* The authors are greatly appreciative to the participants of the World Weather Research
519 Program Research Development Project and Forecast Demonstration Project, International Collaborative
520 Experiments for Pyeongchang 2018 Olympic and Paralympic winter games (ICE-POP 2018), hosted by the
521 Korea Meteorological Administration. The authors would also like to thank Josué Gehring, Nikola Besic, and
522 Alfonso Ferrone for their contribution to the operation and maintenance of the MXPol radar and for providing
523 the hydrometeor classification product (<https://doi.org/10.1594/PANGAEA.918315>, Besic et al., 2018;
524 Gehring et al., 2020a; Gehring et al., 2021) and to thank Petersen Walter A and Ali Tokay for their contribution
525 to the Parsivel data product (Petersen et al., 2019).

526

527 **References**

- 528 Alcott, T. I., and Steenburgh, W. J.: Orographic influences on a Great Salt Lake–effect snowstorm, Mon.
529 Weather Rev.,141, 2432-2450, <https://doi.org/10.1175/MWR-D-12-00328.1>, 2013.
- 530 Bae, S. Y., Hong, S. Y., and Tao, W. K.: Development of a single-moment cloud microphysics scheme with
531 prognostic hail for the Weather Research and Forecasting (WRF) model, Asia-Pacific J. Atmos. Sci.,
532 55, 233-245, <https://doi.org/10.1007/s13143-018-0066-3>, 2019.
- 533 Bao, J.-W., Michelson, S. A., and Grell, E. D.: Microphysical process comparison of three microphysics
534 parameterization schemes in the WRF model for an idealized squall-line case study, Mon. Weather Rev.,
535 147, 3093-3120, <https://doi.org/10.1175/MWR-D-18-0249.1>, 2019.
- 536 Basic, N., Gehring, J., Praz, C., Figueras i Ventura, J., Grazioli, J., Gabella, M., Germann, U., and Berne, A.:
537 Unraveling hydrometeor mixtures in polarimetric radar measurements, Atmos. Meas. Tech., 11, 4847–
538 4866, <https://doi.org/10.5194/amt-11-4847-2018>, 2018.
- 539 Boudala, F. S., Isaac, G. A., Rasmussen, R., Cober, S. G., and Scott, B.: Comparison of snowfall
540 measurements in complex terrain made during the 2010 Winter Olympics in Vancouver, Pure Appl.
541 Geophys., 171, 113-127, <https://doi.org/10.1007/s00024-012-0610-5>, 2014.
- 542 Chen, F., and Dudhia, J.: Coupling an advanced land surface–hydrology model with the Penn State–NCAR
543 MM5 modeling system. Part I: Model implementation and sensitivity, Mon. Weather Rev., 129, 569–
544 585, [https://doi.org/10.1175/1520-0493\(2001\)129<0569:CAALSH>2.0.CO;2](https://doi.org/10.1175/1520-0493(2001)129<0569:CAALSH>2.0.CO;2), 2001.
- 545 Cheong, S.-H., Byun, K.-Y., and Lee, T.-Y.: Classification of snowfalls over the Korean Peninsula based on
546 developing mechanism, Atmosphere, 16, 33-48, 2006.
- 547 Choi, G., and Kim, J.: Surface synoptic climatic patterns for heavy snowfall events, J. Korean Geogr. Soc.,
548 45, 319-341, 2010.

- 549 [Conrick, R., and Mass, C. F.: Evaluating simulated microphysics during OLYMPEX using GPM satellite](#)
550 [observations, *J. Atmos. Sci.* 76, 1093-1105, <https://doi.org/10.1175/JAS-D-18-0271.1>, 2019](#)
- 551 Das, S. K., Hazra, A., Deshpande, S. M., Krishna, U. M., and Kolte, Y. K.: Investigation of cloud
552 microphysical features during the passage of a tropical mesoscale convective system: Numerical
553 simulations and X-band radar observations, *Pure Appl. Geophys.*, ___-178, 185–204,
554 <https://doi.org/10.1007/s00024-020-02622-w>, 2021.
- 555 Dee, D. P., and coauthors: The ERA-Interim reanalysis: configuration and performance of the data
556 assimilation system. *Q. J. R. Meteorol. Soc.*, 137, 553–597, <https://doi.org/10.1002/qj.828>, 2011.
- 557 Dudhia, J., Hong, S. Y., Lim, K. S.: A new method for representing mixed-phase particle fall speeds in bulk
558 microphysics parameterization, *J. Meteorol. Soc. Jpn.*, 86, 33-44, <https://doi.org/10.2151/jmsj.86A.33>,
559 2008.
- 560 Fan, J., and coauthors: -Cloud-resolving model intercomparison of an MC3E squall line case: Part 1-
561 Convective updrafts, *J. Geophys. Res. Atmos.*, 122, 9351–9378, <https://doi.org/10.1002/2017JD026622>,
562 2017.
- 563 Geerts, B., Yang, Y., Rasmussen, R., Haimov, S., and Pokharel, B.: Snow growth and transport patterns in
564 orographic storms as estimated from airborne vertical-plane dual-doppler radar data, *Mon. Weather*
565 *Rev.*, 143, 644-665, <https://doi.org/10.1175/MWR-D-14-00199.1>, 2015.
- 566 Gehring, J., Ferrone, A., Billault-Roux, A. C., Besic, N., and Berne, A.: Radar and ground-level measurements
567 of precipitation during the ICE-POP 2018 campaign in South-Korea, *PANGAEA*,
568 <https://doi.org/10.1594/PANGAEA.918315>, 2020a.
- 569 Gehring, J., Oertel, A., Vignon, É., Jullien, N., Besic, N., and Berne, A.: Microphysics and dynamics of
570 snowfall associated with a warm conveyor belt over Korea, *Atmos. Chem. Phys.*, 20, 7373–7392,
571 <https://doi.org/10.5194/acp-20-7373-2020>, 2020b.

572 Gehring, J., Ferrone, A., Bilault-Roux, A.-C., Besic, N., Anh, K. D., Lee, G., and Berne, A.: Radar and ground-
573 level measurements of precipitation collected by the École Polytechnique Fédérale de Lausanne during
574 the International Collaborative Experiments for PyeongChang 2018 Olympic and Paralympic winter
575 games. *Earth Syst. Sci. Data*, 13, 417–433, <https://doi.org/10.5194/essd-13-417-2021>, 2021.

576 Goodison, B. E., Louie P. Y. T., and Yang, D.: WMO solid precipitation measurement intercomparison, 1998.

577 Han, M., Braun, S. A., Matsui, T., and Williams, C. R.: Evaluation of cloud microphysics schemes in
578 simulations of a winter storm using radar and radiometer measurements, *J. Geophys. Res. Atmos.*, 118,
579 1401–1419, <https://doi.org/10.1002/jgrd.50115>, 2013.

580 Hong, S. Y., Noh, Y., and Dudhia, J.: A new vertical diffusion package with an explicit treatment of
581 entrainment processes, *Mon. Weather Rev.*, 134, 2318–2341, <https://doi.org/10.1175/MWR3199.1>,
582 2006

583 Huang, Y., Wang, Y., Xue, L., Wei, X., Zhang, L., and Li, H.: Comparison of three microphysics
584 parameterization schemes in the WRF model for an extreme rainfall event in the coastal metropolitan
585 City of Guangzhou, China, *Atmos. Res.*, 240, 104939, <https://doi.org/10.1016/j.atmosres.2020.104939>,
586 2020.

587 Iacono, M. J., Delamere, J. S., Mlawer, E. J., Shephard, M. W., Clough, S. A., and Collins, W. D.: Radiative
588 forcing by long-lived greenhouse gases: Calculations with the AER radiative transfer models, *J.*
589 *Geophys. Res.*, 113, D13103, <https://doi.org/10.1029/2008JD009944>, 2008.

590 Jang, S., Lim, K. S. S., Ko, J., Kim, K., Lee, G., Cho, S. J., Ahn, K. D., and Lee, Y. H.: Revision of WDM7
591 microphysics scheme and evaluation for precipitating convection over the Korean peninsula, *Remote*
592 *Sens.*, 13, 3860, <https://doi.org/10.3390/rs13193860>, 2021.

593 Jeoung, H., Liu, G., Kim, K., Lee, G., and Seo, E.-K.: Microphysical properties of three types of snow clouds:
594 implication for satellite snowfall retrievals, *Atmos. Chem. Phys.*, 20, 14491–14507,
595 <https://doi.org/10.5194/acp-20-14491-2020>, 2020.

596

597 Jiménez, P. A., Dudhia, J., González-Rouco, J. F., Navarro, J., Montávez, J. P., and García-Bustamante, E.:
598 A revised scheme for the WRF surface layer formulation, *Mon. Weather Rev.*, 140, 898–918,
599 <https://doi.org/10.1175/MWR-D-11-00056.1>, 2012.

600 Kain, J. S. and Fritsch, J. M.: A one-dimensional entraining/detraining plume model and its application in
601 convective parameterization, *J. Atmos. Sci.* 47:2784–2802, 1990.

602 Kain, J. S.: The Kain–Fritsch convective parameterization: an update, *J. Appl. Meteorol. Climatol.*, 43, 170–
603 181, [https://doi.org/10.1175/1520-0450\(2004\)043<0170:TKCPAU>2.0.CO;2](https://doi.org/10.1175/1520-0450(2004)043<0170:TKCPAU>2.0.CO;2), 2004.

604 Kim, Y. J., Kim, B. G., Shim, J. K., and Choi, B. C.: Observation and numerical simulation of cold clouds
605 and snow particles in the Yeongdong region, *Asia Pac. J. Atmos. Sci.*, 54, 499–510,
606 <https://doi.org/10.1007/s13143-018-0055-6>, 2018.

607 Kim, K., Bang, W., Chang, E., Tapiador, F. J., Tsai, C., Jung, E., and Lee, G.: Impact of wind pattern and
608 complex topography on snow microphysics during International Collaborative Experiment for
609 PyeongChang 2018 Olympic and Paralympic winter games (ICE-POP 2018). *Atmos. Chem. Phys.*, 21,
610 11955–11978, <https://doi.org/10.5194/acp-21-11955-2021>, 2021a.

611 Kim, Y. J., In, S. R., Kim, H. M., Lee, J. H., Kim, K. R., Kim, S., and Kim, B. G.: Sensitivity of snowfall
612 characteristics to meteorological conditions in the Yeongdong region of Korea, *Adv. Atmos. Sci.*, 38,
613 413–429, <https://doi.org/10.1007/s00376-020-0157-9>, 2021b.

614 Kim, K. B., and Lim, K.-S. S.: The numerical error in WDM6 and its impacts on the simulated precipitating
615 convections, AOGS 18h Annual Meeting, Asia Oceanic Geoscience Society, AS23-A005, 2021.

616 Kochendorfer, J., and coauthors: Analysis of single-Alter-shielded and unshielded measurements of mixed
617 and solid precipitation from WMO-SPICE, *Hydrol. Earth Syst. Sci.*, 21, 3525–3542,
618 <https://doi.org/10.5194/hess-21-3525-2017>, 2017.

619 Lei, H., Guo, J., Chen, D., and Yang, J.: Systematic bias in the prediction of warm-rain hydrometeors in the
620 WDM6 microphysics scheme and modifications, *J. Geophys. Res.*, 125,
621 <https://doi.org/10.1029JD030756>, 2020.

622 [Lim, K. S. S., and Hong, S. Y.: Development of an effective double-moment cloud microphysics scheme with
623 prognostic cloud condensation nuclei \(CCN\) for weather and climate models, *Mon. Weather Rev.*, 138,
624 1587-1612, <https://doi.org/10.1175/2009MWR2968.1>, 2010.](#)

625 Lim, K. S. S., Chang, E.-C., Sun, R., Kim, K., Tapiador, F. J., and Lee, G.: Evaluation of simulated winter
626 precipitation using WRF-ARW during the ICE-POP 2018 field campaign, *Wea. Forecasting*, 35, 2199–
627 2213, <https://doi.org/10.1175/WAF-D-19-0236.1>, 2020.

628 Liu, C., and Moncrieff, M. W.: Sensitivity of cloud-resolving simulations of warm-season convection to cloud
629 microphysics parameterizations, *Mon. Weather Rev.*, 135, 2854–2868,
630 <https://doi.org/10.1175/MWR3437.1>, 2007.

631 Liou, Y.-C., and Chang, Y.-J.: Variational multiple-doppler radar three-dimensional wind synthesis method
632 and its impacts on thermodynamic retrieval, *Mon. Weather Rev.*, 137, 3992–4010,
633 <https://doi.org/10.1175/2009MWR2980.1>, 2009.

634 [Löffler-Mang, M., and Joss, J.: An optical disdrometer for measuring size and velocity of hydrometeors, *J.*
635 *Atmos. Ocean. Technol.*, 17, 130-139, <https://doi.org/10.1175/2009MWR2968.1>, 2000.](#)

636 Luo, Y., Wang, Y., Wang, H., Zheng, Y., and Morrison, H.: Modeling convective-stratiform precipitation
637 processes on a Mei-Yu front with the Weather Research and Forecasting model: Comparison with
638 observations and sensitivity to cloud microphysics parameterizations, *J. Geophys. Res.*, 115,
639 <https://doi.org/10.1029/2010JD013873>, 2010.

640 [Ma, Z., and coauthors: Sensitivity of snowfall forecast over North China to ice crystal deposition/sublimation
641 parameterizations in the WSM6 cloud microphysics scheme, *Q. J. R. Meteorol. Soc.* 147, 3349-3372,
642 <https://doi.org/10.1002/qj.4132>, 2021.](#)

643 McMillen, J. D., and Steenburgh, W. J.: Impact of microphysics parameterizations on simulations of the 27
644 October 2010 Great Salt Lake-effect snowstorm, *Wea. Forecasting*, 30, 136-152,
645 <https://doi.org/10.1175/WAF-D-14-00060.1>, 2015.

646 Min, K.-H., Choo, S., Lee, D., and Lee, G.: Evaluation of WRF cloud microphysics schemes using radar
647 observations, *Wea. Forecasting*, 30, 1571-1589, <https://doi.org/10.1175/WAF-D-14-00095.1>, 2015.

648 ~~Molthan, A. L., and Colle, B. A.: Comparisons of single- and double-moment microphysics schemes in the
649 simulation of a synoptic-scale snowfall event, *Mon. Weather Rev.*, 140, 2982-3002,
650 <https://doi.org/10.1175/MWR-D-11-00292.1>, 2012.~~

651 ~~Molthan, A. L., Colle, B. A., Yuter, S. E., and Stark, D.: Comparisons of modeled and observed reflectivities
652 and fall speeds for snowfall of varied riming degrees during winter storms on Long Island, New York,
653 *Mon. Weather Rev.*, 144, 4327-4347, <https://doi.org/10.1175/MWR-D-15-0397.1>, 2016~~

654 ~~Moretette, J., Barker, H. W., Cole, J. N. S., Iacono, M. J., and Pincus, R.: Impact of a new radiation package,
655 McRad, in the ECMWF integrated forecasting system, *Mon. Weather Rev.*, 136, 4773-4798,
656 <https://doi.org/10.1175/2008MWR2363.1>, 2008.~~

657 Morrison, H., and Grabowski, W. W.: Comparison of bulk and bin warm-rain microphysics models using a
658 kinematic framework, *J. Atmos. Sci.*, 64, 2839-2861, <https://doi.org/10.1175/JAS3980>, 2007.

659 Morrison, H. and Milbrandt, J.: Comparison of two-moment bulk microphysics schemes in idealized supercell
660 thunderstorm simulations, *Mon. Weather Rev.* 139, 1103-1130,
661 <https://doi.org/10.1175/2010MWR3433.1>, 2011

662 Nam, H.-G., Kim, B.-G., Han, S.-O., Lee, C., and Lee, S.-S.: Characteristics of easterly-induced snowfall in
663 Yeongdong and its relationship to air-sea temperature difference, *Asia-Pac. J. Atmos. Sci.*, 50, 541-
664 552, <https://doi.org/10.1007/s13143-014-0044-3>, 2014.

665 Park, S. K., and Park, S.: On a flood-producing coastal mesoscale convective storm associated with the
666 kor'easterlies: Multi-Data analyses using remotely-sensed and in-situ observations and storm-scale
667 model simulations, *Remote Sens.*, 12, 1–25, <https://doi.org/10.3390/RS12091532>, 2020.

668 Petersen, Walter A and Ali Tokay: GPM Ground Validation Autonomous Parsivel Unit (APU) ICE
669 POP [indicate subset used]. Dataset available online from the NASA Global Hydrology Resource
670 Center DAAC, Huntsville, Alabama, U.S.A.,
671 <http://dx.doi.org/10.5067/GPMGV/ICEPOP/APU/DATA101>, 2019.

672 Rasmussen, R., and coauthors: How well are measuring snow: The NOAA/FAA/NCAR winter precipitation
673 test bed, *Bull. Am. Meteorol. Soc.*, 93, 811-829, <https://doi.org/10.1175/BAMS-D-11-00052.1>, 2012.

674 Rezacova, D., P. Zacharov, and Z. Sokol: Uncertainty in the area-related QPF for heavy convective
675 precipitation, *Atmos. Res.*, **93**, 238–246,
676 <https://doi.org/10.1016/j.atmosres.2008.12.005>, [doi:10.1016/j.atmosres.2008.12.005](https://doi.org/10.1016/j.atmosres.2008.12.005), 2009

서식 지정함: 글꼴: 기움임플 없음

677 Skamarock, W. C., and coauthors: A description of the advanced research WRF version 3 (2008) NCAR
678 Technical Note, NCAR, Boulder, CO, 2008.

서식 지정함: 글꼴 색: 자동

679 Smith, C. D., Ross, A., Kochendorfer, J., Earle, M. E., Wolff, M., Buisán, S., Roulet Y., A., and Laine, T.:
680 Evaluation of the WMO solid precipitation intercomparison experiment (SPICE) transfer functions for
681 adjusting the wind bias in solid precipitation measurements, *Hydrol. Earth Syst. Sci.*, 24,4025-4043,
682 <https://doi.org/10.5194/hess-24-4025-2020>, 2020.

683 Solomon, A., Morrison, H., Persson, O., Shupe, M. D., and Bao, J. W.: Investigation of microphysical
684 parameterizations of snow and ice in Arctic clouds during M-PACE through model-observation
685 comparisons, *Mon. Weather Rev.*, 137, 3110-3128, <https://doi.org/10.1175.2009MWR2688.1>, 2009.

686 Steenburgh, W. J., and Nakai, S.: Perspectives on sea-and lake-effect precipitation from Japan's "Gosetsu
687 Chitai", *Bull. Am. Meteorol. Soc.*, 101, E58–E72, <https://doi.org/10.1175/BAMS-D-18-0335.1>, 2020.

- 688 Thompson, G., and Eidhammer, T.: A study of aerosol impacts on clouds and precipitation development in a
689 large winter cyclone, *J. Atmos. Sci.*, 71, 3636-3658, <https://doi.org/10.1175/JAS-D-13-0305.1>, 2014.
- 690 Tokay, A., Hartmann, P., Battaglia, A., Gage, K. S., Clark, W. L., and Williams, C. R.: A field study of
691 reflectivity and Z-R relations using vertically pointing radars and disdrometers, *J. Atmos. Ocean.*
692 *Technol.*, 26, 1120-1134, <https://doi.org/10.1175/2008JTECHA1163.1>, 2009.
- 693 Tsai, C., Kim, K., Liou, Y., Lee, G., and Yu, C.: Impacts of topography on airflow and precipitation in the
694 Pyeongchang area seen from Multiple-Doppler Radar observations, *Mon. Weather Rev.*, 146, 3401–
695 3424, <https://doi.org/10.1175/MWR-D-17-0394.1>, 2018.
- 696 Veals, P. G., Steenburgh, W. J., Nakai, S., and Yamaguchi, S.: Factors affecting the inland and orographic
697 enhancement of sea-effect snowfall in the Hokuriku region of Japan, *Mon. Weather Rev.*, 147, 3121–
698 3143, <https://doi.org/10.1175/MWR-D-19-0007.1>, 2019.
- 699 Vignon, É., Besic, N., Jullien, N., Gehring, J., Berne, A.: Microphysics of snowfall over coastal east antarctica
700 simulated by polar WRF and observed by radar, *J. Geophys. Res. Atmos.*, 124, 11452-11476,
701 <https://doi.org/10.1029/2019JD031028>, 2019.

703 **Figure and Table captions**

704 **Table 1.** Eight selected snowfall events during the International Collaborative Experiment held at the
705 Pyeongchang 2018 Olympics and Winter Paralympic Games (ICE-POP 2018) field campaign and their
706 characteristics, obtained from the automatic weather station (AWS) by the Korea Meteorological
707 Administration (KMA). Forecast and analysis periods are also noted.

708 **Table 2.** Summary of the Weather Research and Forecasting (WRF) model configurations.

709 **Table 3.** Four bulk-type cloud microphysics parameterizations and their prognostic variables. The existence
710 of prognostic variables in each parameterization is denoted with the symbol “o” (existence) or “x”
711 (nonexistence). N_x and Q_x represent the number concentration and mixing ratio of a hydrometeor, X. The
712 subscript, C, R, I, S, G, and H, indicates cloud water, rain, cloud ice crystal, snow, graupel, and hail,
713 respectively.

714 **Table 4.** List of symbols for cloud microphysical processes in each microphysics scheme and their meaning.
715 The symbol used differently in each scheme is reconciled in our study, addressed in the row, “Notation.”

716 **Figure 1.** Observed accumulated precipitation amount [mm] (a) for 21-h from 0300 UTC 22 to 0000 UTC 23
717 January (CASE 3), (b) for 29-h from 0500 UTC 07 to 1000 UTC 08 March (CASE 6), and (c) for 10-h from
718 0800 UTC 15 to 1800 UTC 15 March (CASE 7), obtained from the AWS. The location of one coastal site,
719 Gangneung-Wonju National University (GWU) and three mountain sites, BoKwang 1-ri Community Center
720 (BKC), DaeGwallyeong regional Weather office (DGW) and MayHills Supersite (MHS) is noted in Figure
721 1(a). **Figure 2.** Normalized frequency of the measured precipitation particle fall velocity as a function of
722 diameters at GWU (upper panel) and DGW (lower panel) sites. (a), (d) are for CASE 3, (b), (e) for CASE 6,
723 and (c), (f) for CASE 7 during the analysis period. The solid lines represent the relationship between the fall
724 velocity and diameter for rain (the power law fit the Gunn and Kinzer (1949) data (Atlas et al., 1973)), dendrite
725 (derived from the observed data (Lee et al., 2015)), graupel, and hail (derived from the observed data
726 (Heymsfield et al., 2018)) at sea level.

727 **Figure 3.** Area of hydrometeor types in which hourly average fraction of hydrometeors is larger than the
728 threshold indicated. Hydrometeor types are derived from X-band Doppler dual polarization radar (MXPoI)

729 along the direction between MHS and GWU sites at (a) 10 UTC 22 Jan (CASE 3), (b) 23 UTC 07 Mar (CASE
730 6), and (c) 14 UTC 15 Mar (CASE 7). Eight hydrometeor categories such as crystal (CR), aggregate (AG),
731 rimed particle (RP), ice hail/graupel (IH), melting hail (MH), wet snow (WS), light rain (LR), and rain (RN)
732 are identified. The Green shade represents the terrain. The flows along the cross-section, retrieved from
733 multiple Doppler radars, are also drawn in each figure and the vertical component of the arrows are upward
734 air motion. The flows and classified hydrometeors are the hourly averaged ones.

735 **Figure 4.** Model domain consisted of the three nested domains with 9-3-1-km resolutions centered on the
736 Korean peninsula. Shading indicates the terrain height [m] above the sea level and latitudes and longitudes
737 are denoted in the margins. The analysis domain is denoted with a dotted square inside of the innermost
738 domain, d03.

739 **Figure 5.** Statistical skill scores of bias, root mean square error (RMSE), probability of detection (POD), and
740 false alarm ratio (FAR) for the simulated precipitation, with respect to the AWS observation. The units of bias
741 and RMSE shown in Figures 5(a) and (b) are [mm]. White, black, yellow, and blue-colored bars represent the
742 results for the simulations with the WDM6, Thompson, and Morrison schemes. The cold-low, warm-low, and
743 air-sea interaction cases are shaded in blue, red, and green color. The total cumulative precipitation [mm] for
744 each case, obtained from the AWS (Table 1), is also noted in Figure 5(a) using red dots together with the scale
745 in the right y-axis.

746 **Figure 6.** Accumulated precipitation [mm] of the simulations using different cloud microphysics
747 parameterizations during the analysis period. (a)–(d) are for CASE 3, (b), (e) for CASE 6, and (c), (f) for
748 CASE 7 during the analysis period. (a)–(d) are for CASE 3, (e)–(h) for CASE 6, and (j)–(l) for CASE7. The
749 simulations in the first and second columns are conducted with the WDM6 and WDM7 schemes. The ones in
750 the third and fourth columns are conducted with the Thompson and Morrison schemes. Black, red, blue, and
751 purple contours represent the rain, snow, graupel, and hail-type precipitation at the surface. The contour
752 intervals for CASE 3, CASE 6, and CASE 7 are 3, 10, and 5 mm. Red, blue, and black contours represent the
753 snow, graupel, and hail type precipitation at the surface. The contour intervals for snow, graupel, and hail are
754 5, 10, and 3 mm.

755 **Figure 7.** Terrain and the simulated hydrometeor mixing ratio [g kg^{-1}] along the cross-section between GWU
756 and MHS sites for (a)–(e) CASE 3, (f)–(j) CASE 6, and (k)–(o) CASE 7. From the left column, figures indicate
757 the simulation results with the WDM6, WDM7, Thompson, and Morrison schemes. Shaded green and blue
758 indicate the cloud water and ice mixing ratios, respectively. Red, blue, and black-solid contours are for the
759 snow, graupel, and hail mixing ratios. The contour levels are in 0.1 g kg^{-1} increments and the contour labels
760 are in $0.1\text{--}0.2 \text{ g kg}^{-1}$ increments. The gray solid line represents the 0°C line. The wind fields are overlaid at
761 the same time.

762 **Figure 8.** Time-domain averaged vertical hydrometeor mixing ratio profiles from the simulations using (a)
763 WDM6, (b) WDM7, (c) Thompson, and (d) Morrison schemes for CASE 3. The averaged time and domain
764 are the same as Figure 6. The sum of snow and cloud ice mixing ratios is drawn with a red line in all
765 simulations.

766 **Figure 9.** Relative contribution of time-domain averaged production tendency term during the analysis period.
767 From the left column, figures indicate the simulation results with the WDM6, WDM7, Thompson, and
768 Morrison schemes. (a)–(d) are the terms for cloud water, (e)–(h) for rain, (i)–(l) for cloud ice, (m)–(p) for
769 snow, and (q)–(t) for graupel, and (u) for hail. The hail is only predicted in WDM7. The scaling number, sum
770 of the absolute value of each production tendency, which corresponds to 100%, are noted in the upper left
771 corner of each figure.

772 **Figure 10.** Same as Figure 8 but representing the results for CASE 6.

773 **Figure 11.** Same as Figure 9 but representing the results for CASE 6.

774 **Figure 12.** Same as Figure 8 but representing the results for CASE 7.

775 **Figure 13.** Same as Figure 9 but representing the results for CASE 7.

779 **Table 1.** Eight selected snowfall events during the International Collaborative Experiment held at the
780 Pyeongchang 2018 Olympics and Winter Paralympic Games field campaign and their characteristics, obtained
781 from the Automatic Weather Station by the Korea Meteorological Administration. Forecast and analysis
782 periods are also noted.

	Forecast Period [UTC]	Analysis Period [UTC]	Accumulated Precipitation [mm]	Maximum Rain Rate [mm h ⁻¹]	Synoptic Feature
CASE 1	2017.11.24.1200–26.1200	2017.11.24.20000–26.0000	32.09	13.23	Cold Low
CASE 2	2017.12.23.1200–24.1800	2017.12.23.2000–24.1200	18.60	6.45	Warm Low
CASE 3	2018.01.22.0000–23.0600	2018.01.22.0300–23.0000	6.03	2.41	Cold Low
CASE 4	2018.02.27.1800–03.01.0000	2018.02.27.2300–28.1800	57.12	10.19	Warm Low
CASE 5	2018.03.04.0000–05.1200	2018.03.04.0800–05.0900	55.17	13.65	Warm Low
CASE 6	2018.03.07.0000–08.1200	2018.03.07.0500–08.1000	33.07	3.93	Warm Low
CASE 7	2018.03.15.0000–16.0000	2018.03.15.0800–15.1800	25.52	4.87	Air-sea interaction
CASE 8	2018.03.20.1200–21.1800	2018.03.20.1800–21.1400	25.83	3.186	Warm Low

783

784

785 **Table 2.** Summary of the Weather Research and Forecasting (WRF) model configuration.

786

	WRF v4.1.3			Reference
	Domain 1	Domain 2	Domain 3	
Number of grid (x × y × z)	169 × 169 × 65	294 × 348 × 65	330 × 339 × 65	
Cumulus	Kain-Fritsch			Kain and Fritsch, 1990; Kain, 2004
PBL	Yonsei University Scheme			Hong et al., 2006
Surface layer	Revised MM5 Monin-Obukhov scheme			Jiménez et al., 2012
Land surface	Unified Noah Land Surface Model			Chen and Dudhia 2001
Long/short wave radiation	Rapid Radiative Transfer Model for General Circulation Models			Iacono et al., 2008; Morcrette et al., 2008
Initial/boundary conditions	ERA-interim 0.75 Degree			Dee et al., 2011

787

788 **Table 3.** Four bulk-type cloud microphysics parameterizations and their prognostic variables. The existence
789 of prognostic variables in each parameterization is denoted with “O” (existence) or “X” (nonexistence). N_X
790 and Q_X represent the number concentration and mixing ratio of a hydrometeor, X. The subscript, C, R, I, S,
791 G, and H, indicates cloud water, rain, cloud ice crystal, snow, graupel, and hail, respectively.

Parameterization (Reference)	N_C	Q_C	N_R	Q_R	N_I	Q_I	N_S	Q_S	N_G	Q_G	N_H	Q_H
WDM6 (Lim and Hong, 2010)	O	O	O	O	X	O	X	O	X	O	X	X
WDM7 (Bae et al., 2018 2019)	O	O	O	O	X	O	X	O	X	O	X	O
Thompson (Thompson et al., 2008)	X	O	O	O	O	O	X	O	X	O	X	X
Morrison (Morrison et al., 2005)	X	O	O	O	O	O	O	O	O	O	X	X

793

794 **Table 4.** List of symbols for cloud microphysical processes in each microphysics scheme and their meaning.

795 The symbol used differently in each scheme is reconciled in our study, addressed in the row, “Notation.”

796

Hydrometeor	Notation	Source/sink processes for each microphysics scheme				Meaning
		WDM6 WDM6	WDM7	Thompson	Morrison	
Cloud water	QCCON	pcond	pcond	prw_vcd	pcc	Condensation/evaporation of cloud water
	QCGEN	pcact	pcact	-	-	CCN activation
	QRAUT	praut, prevp_s	praut, prevp_s	prr_wau	prc	Conversion from cloud water to rain
	QCFRZ	pihtf, pihmf	pihtf, pihmf	pri_wfz, pri_hmf	mnuccc, pihmf	Freezing of cloud water
	QCACR	pracw	pracw	prr_rcw	pra	Accretion between cloud water and rain
	QCACI	-	-	-	psacwi	Accretion between cloud water and ice
	QCACS	paacw(T≤0°C)	paacw(T≤0°C)	prs_scw, prg_scw	psacws, pgsacw	Accretion between cloud water and snow
	QCACG	paacw(T≤0°C)	paacw(T≤0°C)	prg_gcw	psacwg	Accretion between cloud water and graupel
	QCACH	-	Phacw	-	-	Accretion between cloud water and hail
	QCWET FORWET	paacw, paacw(T≥0°C)	paacw, paacw, phaew(T≥0°C)	-	-	Wet growth and shedding
QCMUL	-	-	-	qmults, qmultg	Ice multiplication	
QCMLT	pimlt	pimlt	prw_uml	-	Melting to cloud water	
Rain	QRAUT	praut, prevp_s	praut, prevp_s	prr_wau	prc	Conversion from cloud water to rain
	QRCON	prevp	prevp	prv_rev	pre	Condensation/evaporation of rain
	QCACR	pracw	pracw	prr_rcw	pra	Accretion between cloud water and rain
	QRACI	piacr	piacr	prr_rci	piacr, piacrs	Accretion between rain and ice

	QRACS	psacr, pseml	psacr, pseml	pr_rcs	pracs	Accretion between rain and snow
	QRACG	pgacr, pgeml	pgacr, pgeml	pr_rcg	pracg	Accretion between rain and graupel
	QRACH	-	phacr, pheml	-		Accretion between rain and hail
	QRFZ	pgrfz	Pgrfz	pri_rfz, prg_rfz	mnuccl, phsmf, pghmf	Freezing of rain
	QRMUL	-	-	-	qmultr, qmultrg	Ice multiplication by rain
	QRMLT	psmlt, pgmlt	psmlt, pgmlt, phmlt	pr_r_sml, pr_r_gml	pimlt, psmlt, pgmlt	Melting to rain
	QRWET	paacw, paacw(T≥0°C)	paacw, paacw, phacw(T≥0°C)	-		Wet growth and shedding
Cloud ice	QIGEN	pigen	pigen	pri_aha, pri_inu	mnuccl	Ice nucleation
	QIDEP	pidep	pidep	pri_ide	prd, eprd	Deposition/sublimation of ice
	QIMUL	-	-	pri_ahm	qmultr, qmultg, qmultrg	Ice multiplication
	QIFZ	pihmf, pihtf	pihmf, pihtf	pri_wfz, pri_hmf, pri_rfz	mnuccl, pihmf	Freezing to ice
	QSAUT	psaut	psaut	pr_s_iau	prci	Conversion to snow
	QCACI	-	-	-	psacwi	Accretion between cloud water and ice
	QRACI	praci	praci	pri_rci	praci, pracis	Accretion between rain and ice
	QIACS	psaci	psaci	pr_s_sci	prai	Accretion between ice and snow
	QIACG	pgaci	pgaci	-	-	Accretion between ice and graupel

	QIACH	-	phaci	-	-	Accretion between ice and hail
	QIMLT	pimlt	pimlt	prw_iml	-	Melting from ice
Snow	QSAUT	psaut	psaut	prs_iau	prci	Conversion to snow
	QSDEP	psdep	psdep	prs_sde, prs_ide	prds, eprds	Deposition/sublimation of snow
	QSMUL	-	-	prs_ihm	-	Ice multiplication
	QSFZ	-	-	-	pshmf	Freezing to snow
	QGAUT	pgaut	pgaut	-	-	Conversion to graupel
	QCACS	paacw(T≤0°C)	paacw(T≤0°C)	prs_scw, prg_scw	psacws,pgsacw	Accretion between cloud water and snow
	QRACS	psacrqs, pracs, psem1	psacrqs, pracs, psem1	prs_rcs	pracs, psacr	Accretion between rain and snow
	QIACS	Psaci	psaci	prs_rci	prai	Accretion between ice and snow
	QSACG	-	-	-	-	Accretion between snow and graupel
	QSACH	-	phacs	-	-	Accretion between snow and hail
	QSMILT	psmlt	psmlt	prr_sml	psmlt	Melting from snow
	QRACI	piacrqs, praciqs	piacrqs, praciqs	-	piacrs, racis	Accretion between rain and ice
	QSEVP	psevp	psevp	-	evpms	Evaporation of melting snow
Graupel	QGAUT	pgaut	pgaut	-	-	Conversion to graupel
	QGDEP	pgdep	pgdep	prg_gde	prdg, eprdg	Deposition/sublimation of graupel
	QGMUL	-	-	prg_ihm	-	Ice multiplication
	QGFRZ	pgfrz	pgfrz	prg_rfz	mnuccr, pghmf	Freezing to graupel
	QCACG	paacw(T≤0°C)	paacw(T≤0°C)	prg_gcw	psacwg	Accretion between cloud water and graupel
	QRACG	pgacr, pgeml	pgacrqg, pgeml, pracg	prg_gcr	pracg	Accretion between rain and graupel
	QIACG	pgaci	pgaci	-	-	Accretion between ice and graupel

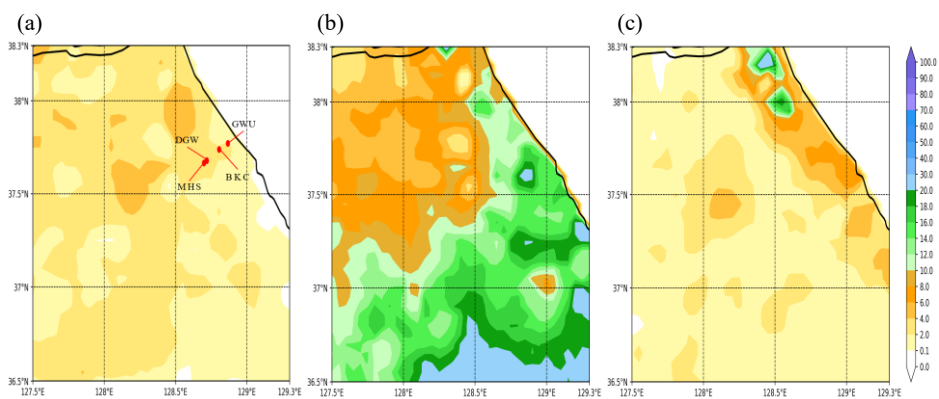
	QSACG	-	-	-	-	Accretion between snow and graupel
	QGACH	-	phacg	-	-	Accretion between graupel and hail
	QGMLT	pgmlt	pgmlt	prg_gml	pgmlt	Melting from graupel
	QCACS	-	-	prg_scw	pgsacw	Accretion between cloud water and snow
	QRACS	piacrqg, praciqg	piacrqg, praciqg	prg_rci	pgracs	Accretion between rain and snow
	QRACI	pracs, psacrqg	pracs, psacrqg	prg_rcs	-	Accretion between rain and ice
	QGEVP	pgevp	pgevp	-	evpmg	Evaporation of melting graupel
	QHAUT	-	phuat	-	-	Conversion to hail
Hail	QHAUT		phaut			Conversion to hail
	QHDEP		phdep			Deposition/sublimation of hail
	QCACH		phacw(T≤0°C)			Accretion between cloud water and hail
	QRACH		phacr, pheml			Accretion between rain and hail
	QIACH		phaci			Accretion between ice and hail
	QSACH		phacs			Accretion between snow and hail
	QGACH		phacg			Accretion between graupel and hail
	QHMLT		phmlt			Melting from hail
	QHEVP		phevp			Evaporation of melting hail
	QRACG		pgacrqh, pracg			Accretion between rain and graupel to hail

797

798

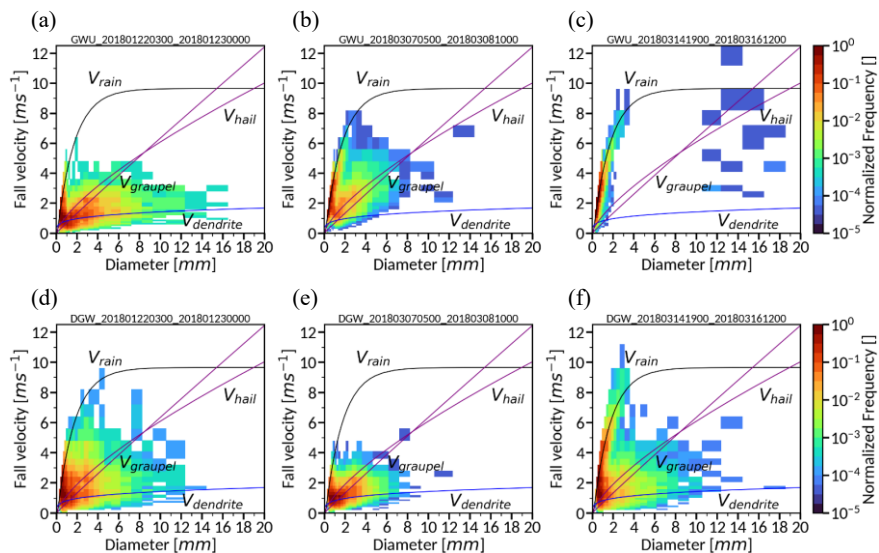
799
800
801
802
803
804
805
806

Figure 1. Observed accumulated precipitation amount [mm] (a) for 21-h from 0300 UTC 22 to 0000 UTC 23 January (CASE 3), (b) for 29-h from 0500 UTC 07 to 1000 UTC 08 March (CASE 6), and (c) for 10-h from 0800 UTC 15 to 1800 UTC 15 March (CASE 7), obtained from the AWS. The location of one coastal site, Gangneung-Wonju National University (GWU) and three mountain sites, BoKwang 1-ri Community Center (BKC), DaeGwallyeong regional Weather office (DGW) and MayHills Supersite (MHS) is noted in Figure 1(a).

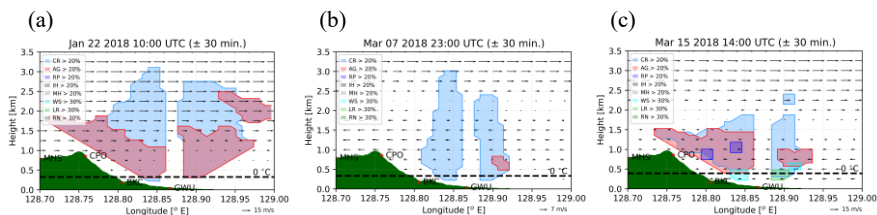


807
808
809
810
811
812
813
814

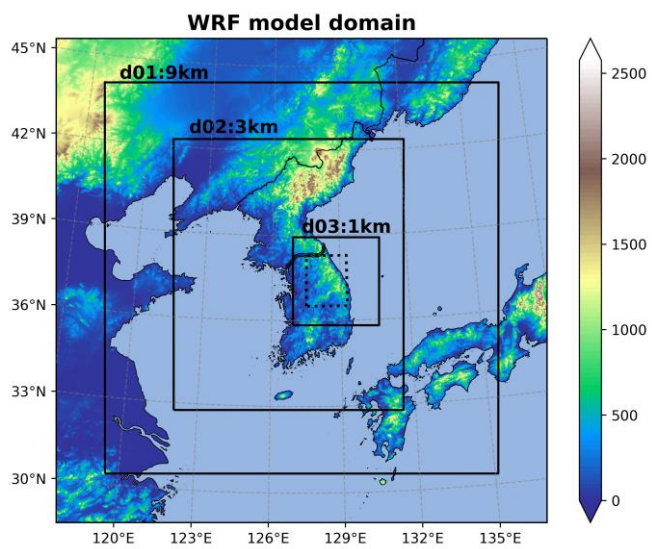
Figure 2. Normalized frequency of the measured precipitation particle fall velocity as a function of diameters at GWU (upper panel) and DGW (lower panel) sites. (a), (d) are for CASE 3, (b), (e) for CASE 6, and (c), (f) for CASE 7 during the analysis period. The solid lines represent the relationship between the fall velocity and diameter for rain (the power law fit the Gunn and Kinzer (1949) data (Atlas et al., 1973)), dendrite (derived from the observed data (Lee et al., 2015)), graupel, and hail (derived from the observed data (Heymsfield et al., 2018)) at sea level.



815 **Figure 3.** Area of hydrometeor types in which hourly average fraction of hydrometeors is larger than the
 816 threshold indicated. Hydrometeor types are derived from X-band Doppler dual-polarization radar (MXPoI)
 817 along the cross-section between MHS and GWU sites at (a) 10 UTC 22 Jan (CASE 3), (b) 23 UTC 07 Mar
 818 (CASE 6), and (c) 14 UTC 15 Mar (CASE 7). Eight hydrometeor categories such as crystal (CR), aggregate
 819 (AG), rimed particle (RP), ice hail/graupel (IH), melting hail (MH), wet snow (WS), light rain (LR), and rain
 820 (RN) are identified. The flows along the cross-section, retrieved from multiple Doppler radars, are also drawn
 821 in each figure and the vertical component of the arrows are upward air motion. The flows and classified
 822 hydrometeors are the hourly averaged ones.

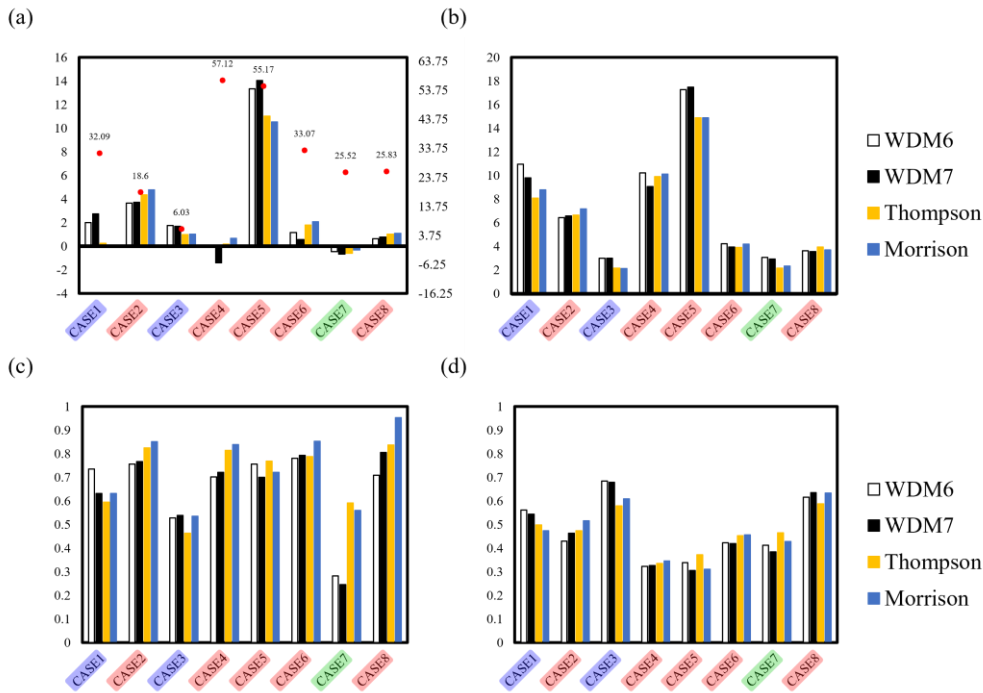


825 **Figure 4.** Model domain consisted of the three nested domains with 9-3-1-km resolutions centered on the
826 Korean peninsula. Shading indicates the terrain height [m] above the sea level and latitudes and longitudes
827 are denoted in the margins. The analysis domain is denoted with a dotted square inside of the innermost
828 domain, d03.



829
830

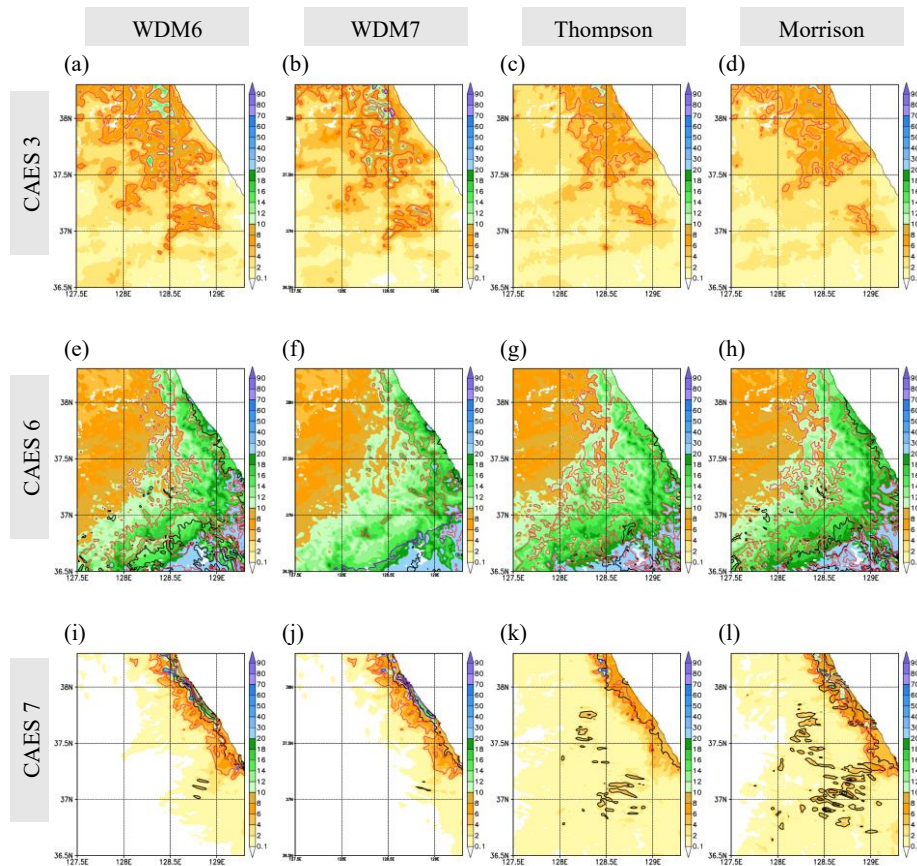
831 **Figure 5.** Statistical skill scores of bias, root mean square error (RMSE), probability of detection (POD), and
 832 false alarm ratio (FAR) for the simulated precipitation, with respect to the AWS observation. The units of bias
 833 and RMSE shown in Figures 5(a) and (b) are [mm]. White, black, yellow, and blue-colored bars represent the
 834 results for the simulations with the WDM6, Thompson, and Morrison schemes. The cold-low, warm-low, and
 835 air-sea interaction cases are shaded in blue, red, and green color. The total cumulative precipitation [mm] for
 836 each case, obtained from the AWS (Table 1), is also noted in Figure 5(a) using red dots together with the scale
 837 in the right y-axis.



838
839

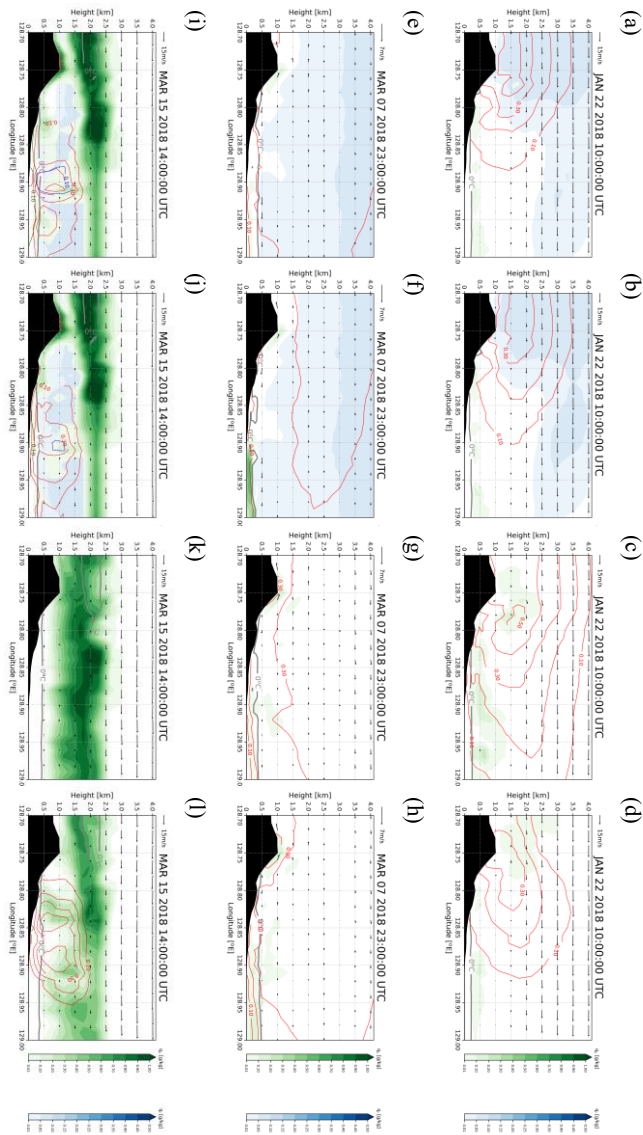
840
841
842
843
844
845
846
847
848
849

Figure 6. Accumulated precipitation [mm] of the simulations using different cloud microphysics parameterizations during the analysis period. (a)–(d) are for CASE 3, (b), (e) for CASE 6, and (c), (f) for CASE 7 during the analysis period. (a)–(d) are for CASE 3, (e)–(h) for CASE 6, and (j)–(l) for CASE 7. The simulations in the first and second columns are conducted with the WDM6 and WDM7 schemes. The ones in the third and fourth columns are conducted with the Thompson and Morrison schemes. Black, red, blue, and purple contours represent the rain, snow, graupel, and hail-type precipitation at the surface. The contour intervals for CASE 3, CASE 6, and CASE 7 are 3, 10, and 5 mm.

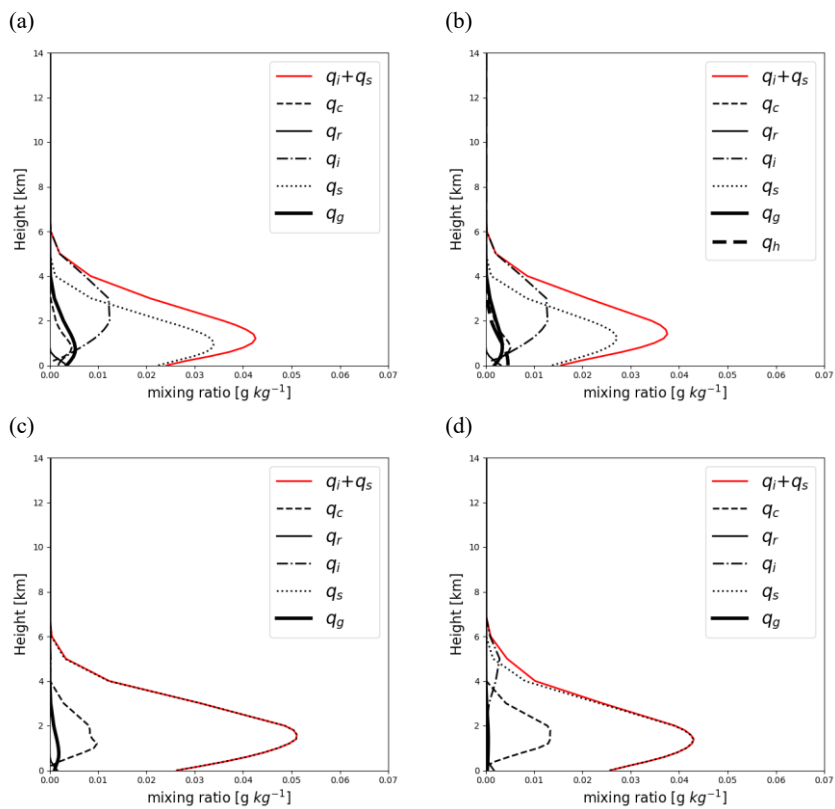


850
851
852
853
854
855
856
857
858
859

Figure 7. Terrain and the simulated hydrometeor mixing ratio [g kg^{-1}] along the cross-section between GWU and MHS sites for (a)–(e) CASE 3, (f)–(j) CASE 6, and (k)–(o) CASE 7. From the left column, figures indicate the simulation results with the WDM6, WDM7, Thompson, and Morrison schemes. Shaded green and blue indicate the cloud water and ice mixing ratios, respectively. Red, blue, and black-solid contours are for the snow, graupel, and hail mixing ratios. The contour levels are in 0.1 g kg^{-1} increments and the contour labels are in $0.1\text{--}0.2 \text{ g kg}^{-1}$ increments. The gray solid line represents the 0°C line. The wind fields are overlaid at the same time.

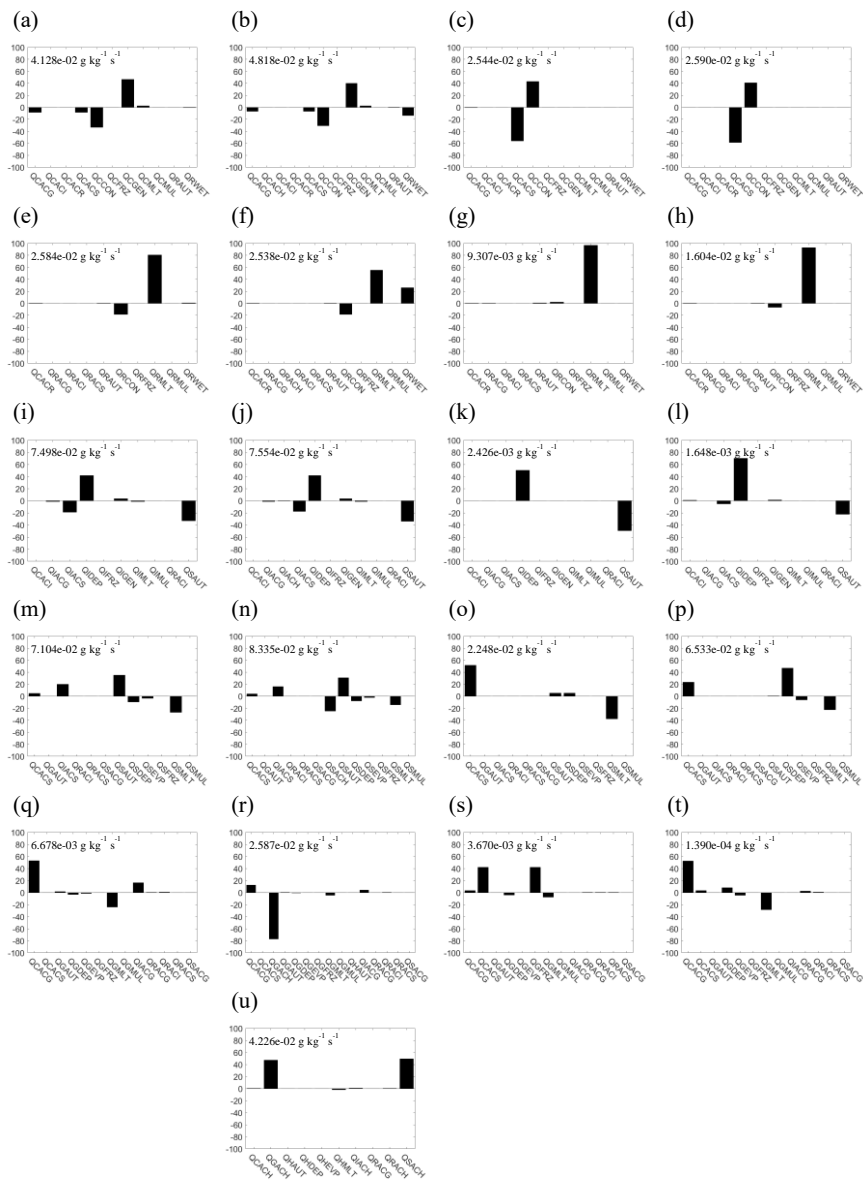


860 **Figure 8.** Time-domain averaged vertical hydrometeor mixing ratio profiles from the simulations using (a)
 861 WDM6, (b) WDM7, (c) Thompson, and (d) Morrison schemes for CASE 3. The averaged time and domain
 862 are the same as Figure 6. The sum of snow and cloud ice mixing ratios is drawn with a red line in all
 863 simulations.
 864
 865



866
867
868
869
870
871
872
873

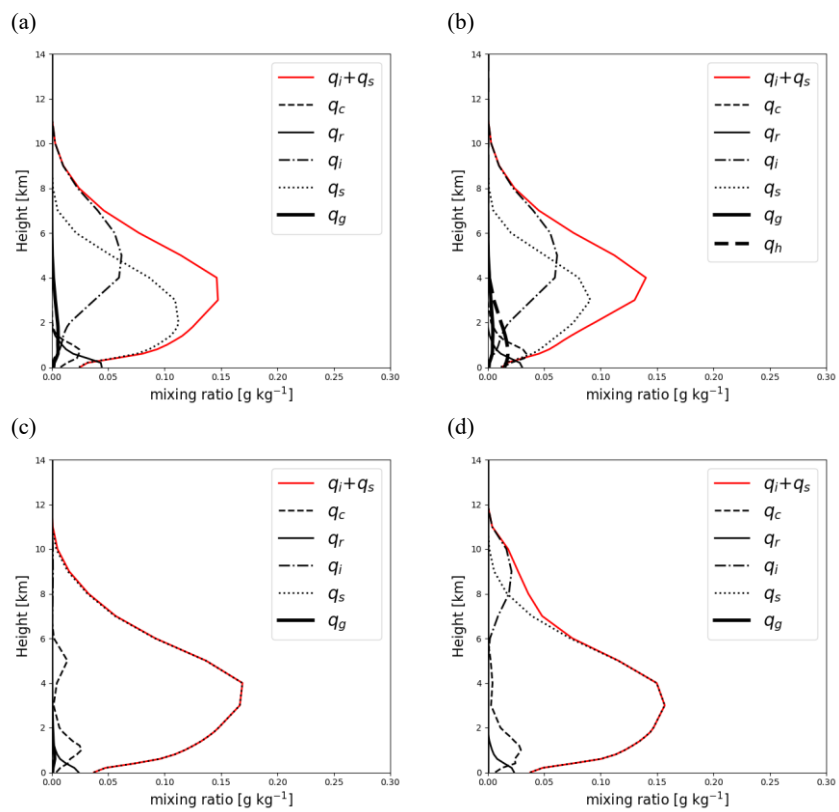
Figure 9. Relative contribution of time-domain averaged production tendency term during the analysis period. From the left column, figures indicate the simulation results with the WDM6, WDM7, Thompson, and Morrison schemes. (a)–(d) are the terms for cloud water, (e)–(h) for rain, (i)–(l) for cloud ice, (m)–(p) for snow, and (q)–(t) for graupel, and (u) for hail. The hail is only predicted in WDM7. The scaling number, sum of the absolute value of each production tendency, which corresponds to 100%, are noted in the upper left corner of each figure.



874 **Figure 10.** Same as Figure 8 but representing the results for CASE 6.

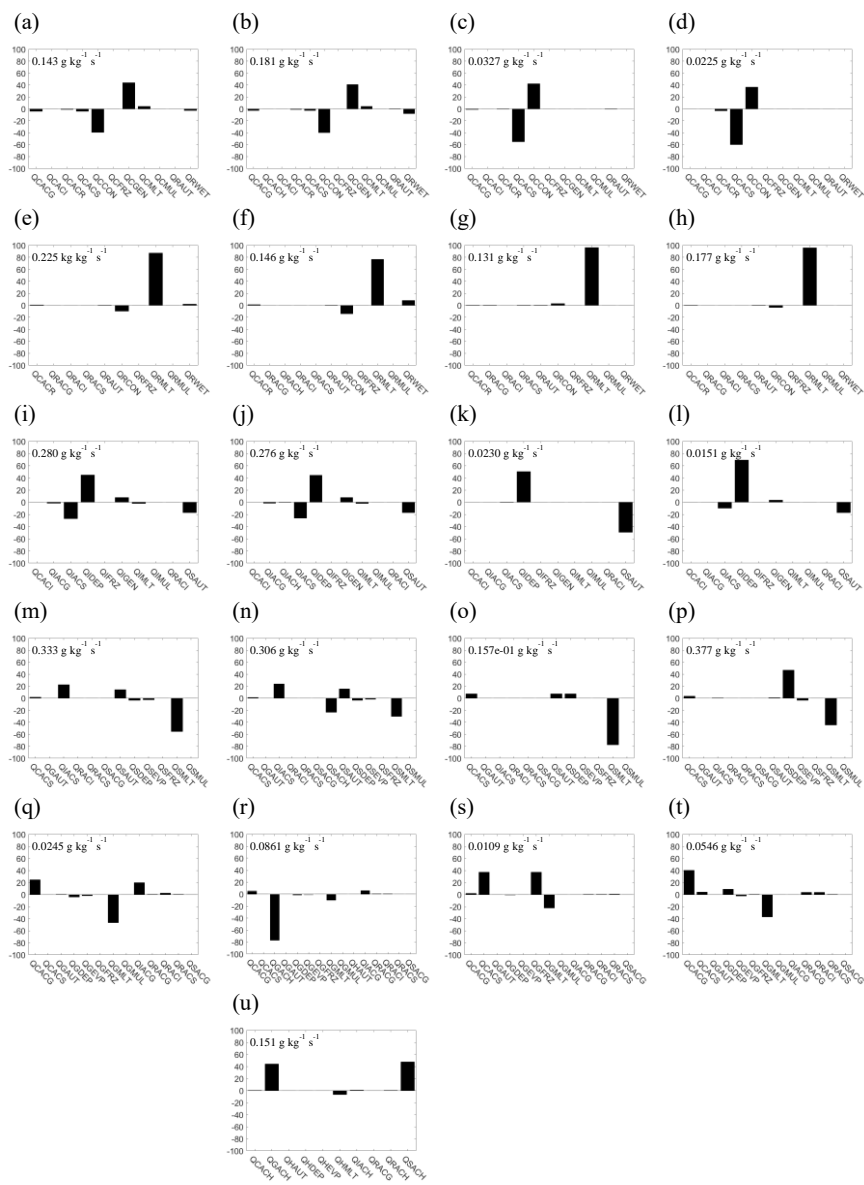
875

876



877 **Figure 11.** Same as Figure 9 but representing the results for CASE 6.

878
879



880 **Figure 12.** Same as Figure 8 but representing the results for CASE 7.

881

882

